
Effective Exploration Based on the Structural Information Principles

Xianghua Zeng¹, Hao Peng¹, Angsheng Li^{1,2}

¹ State Key Laboratory of Software Development Environment, Beihang University, Beijing, China

² Zhongguancun Laboratory, Beijing, China

{zengxianghua, penghao, angsheng}@buaa.edu.cn, liangsheng@gmail.zgclab.edu.cn

Abstract

Traditional information theory provides a valuable foundation for Reinforcement Learning (RL), particularly through representation learning and entropy maximization for agent exploration. However, existing methods primarily concentrate on modeling the uncertainty associated with RL’s random variables, neglecting the inherent structure within the state and action spaces. In this paper, we propose a novel **Structural Information principles-based Effective Exploration** framework, namely **SI2E**. Structural mutual information between two variables is defined to address the single-variable limitation in structural information, and an innovative embedding principle is presented to capture dynamics-relevant state-action representations. The SI2E analyzes value differences in the agent’s policy between state-action pairs and minimizes structural entropy to derive the hierarchical state-action structure, referred to as the encoding tree. Under this tree structure, value-conditional structural entropy is defined and maximized to design an intrinsic reward mechanism that avoids redundant transitions and promotes enhanced coverage in the state-action space. Theoretical connections are established between SI2E and classical information-theoretic methodologies, highlighting our framework’s rationality and advantage. Comprehensive evaluations in the MiniGrid, MetaWorld, and DeepMind Control Suite benchmarks demonstrate that SI2E significantly outperforms state-of-the-art exploration baselines regarding final performance and sample efficiency, with maximum improvements of 37.63% and 60.25%, respectively.

1 Introduction

Reinforcement Learning (RL) has emerged as a pivotal technique for addressing sequential decision-making problems, including game intelligence [Vinyals et al., 2019, Badia et al., 2020], robotic control [Andrychowicz et al., 2017, Liu and Abbeel, 2021], and autonomous driving [Prathiba et al., 2021, Pérez-Gil et al., 2022]. In the realm of RL, striking a balance between exploration and exploitation is crucial for optimizing agent policies and mitigating the risk of suboptimal outcomes, especially in scenarios characterized by high dimensions and sparse rewards [Zhang et al., 2021b].

Recently, advancements in information-theoretic approaches have shown promise for exploration in self-supervised settings. The maximum entropy framework over the action space [Haarnoja et al., 2017] has led to the development of robust algorithms such as Soft Q-learning [Nachum et al., 2017], SAC [Haarnoja et al., 2018], and MPO [Abdolmaleki et al., 2018]. Additionally, various objectives focused on maximizing state entropy are utilized to ensure comprehensive state coverage [Hazan et al., 2019, Islam et al., 2019]. To facilitate the exploration of complex state-action pairs, MaxRenyi optimizes Rényi entropy across the state-action space [Zhang et al., 2021a]. However, a prevalent issue with entropy maximization strategies is their tendency to bias exploration towards low-value states, making them vulnerable to imbalanced state-value distributions in supervised settings. To mitigate

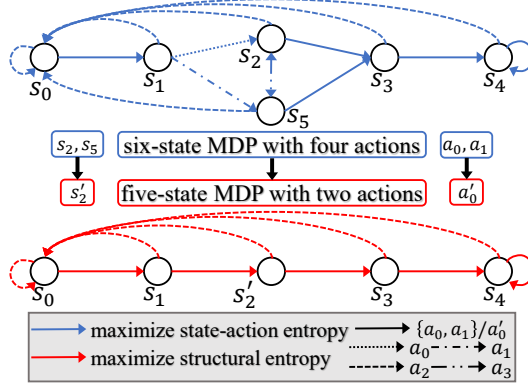


Figure 1: By incorporating the inherent state-action structure, we simplify the original six-state Markov Decision Process (MDP) with four actions to a five-state MDP with two actions, effectively reducing the size of state-action space from $24(6 \times 4)$ to $10(5 \times 2)$. Here, s'_2 and a'_0 represent vertex communities $\{s_2, s_5\}$ and $\{a_0, a_1\}$, respectively. In this scenario, a policy maximizing state-action Shannon entropy would encompass all possible transitions (blue color). In contrast, a policy maximizing structural entropy would selectively focus on crucial transitions (red color), avoiding redundant transitions between s_2 and s_5 .

this, value-conditional state entropy is introduced to compute intrinsic rewards based on the estimated values of visited states [Kim et al., 2023]. Due to their instability in noisy and high-dimensional environments, a Dynamic Bottleneck (DB) [Bai et al., 2021] is developed based on the Information Bottleneck (IB) principle [Tishby et al., 2000], thereby obtaining dynamics-relevant representations of state-action pairs. Despite their successes, existing information-theoretic exploration methods have a critical limitation: they often overlook the inherent structure within state and action spaces. This oversight necessitates new approaches to enhance exploration effectiveness.

Figure 1 illustrates a simple six-state Markov Decision Process (MDP) with four actions. The different densities of the blue and red lines represent different actions, as indicated in the legend, leading to state transitions aimed at optimizing the return to the initial state s_0 . Solid lines specifically denote actions a_0 and a_1 . The transitions between states s_2 and s_5 are deemed redundant as they do not facilitate the primary objective of efficiently returning to s_0 . Therefore, the state-action pairs (s_2, a_3) and (s_5, a_3) have lower policy values. A policy maximizing state-action Shannon entropy would encompass all possible transitions (blue color). In contrast, a policy incorporating the inherent state-action structure will divide these redundant state-action pairs into a vertex sub-community and minimize the entropy of this sub-community to avoid visiting it unnecessarily. Simultaneously, it maximizes state-action entropy, resulting in maximal coverage for transitions (red color) that are more likely to contribute to the desired outcome in the simplified five-state MDP.

Departing from traditional information theory applied to random variables, structural information [Li and Pan, 2016] has been devised to quantify dynamic uncertainty within complex graphs under a hierarchical partitioning structure known as an ‘‘encoding tree’’. Structural entropy is conceptualized as the minimum number of bits required to encode a vertex accessible through a single-step random walk and is minimized to optimize the encoding tree. However, this definition is limited to single-variable graphs and cannot capture the structural relationship between two variables. While the underlying graph can encompass multiple variables, current structural information principles are limited in treating these variables as a single joint variable, measuring only its structural entropy. This limitation prevents the effective quantification of structural similarity between variables, inherently imposing a single-variable constraint. Prior research on reinforcement learning using structural information principles [Zeng et al., 2023b,c] has focused on independently modeling state or action variables without simultaneously considering state-action representations.

In this work, we propose SI2E, a novel and unified framework grounded in structural information principles for effective exploration within high-dimensional and sparse-reward environments. Initially, we embed state-action pairs into a low-dimensional space and present an innovative representation learning principle to capture dynamics-relevant information and compress dynamics-irrelevant information. Then, we strategically increase the state-action pairs’ structural mutual information with subsequent states while decreasing it with current states. We analyze value differences among state-action representations to form a complete graph and minimize its structural entropy to derive the

optimal encoding tree, thereby unveiling the hierarchical community structure of state-action pairs. By leveraging this identified structure, we design an intrinsic reward mechanism tailored to avoid redundant transitions and enhance maximal coverage in exploring the state-action space. Furthermore, we establish theoretical connections between our framework and classical information-theoretic methodologies, highlighting the rationality and advantage of SI2E. Our thorough evaluations across diverse and challenging tasks in the MiniGrid, MetaWorld, and DeepMind Control Suite benchmarks have consistently shown SI2E’s superiority, with significant improvements in final performance and sample efficiency, surpassing state-of-the-art exploration baselines. For further research, the source code is available at ¹. Our contributions are summarized as follows:

- A novel framework based on structural information principles, SI2E, is proposed for effective exploration in high-dimensional RL environments with sparse rewards.
- An innovative principle of structural mutual information is introduced to overcome the single-variable constraint inherent in existing structural information and to enhance the acquisition of dynamics-relevant representations for state-action pairs.
- A unique intrinsic reward mechanism that maximizes the value-conditional structural entropy is designed to avoid redundant transitions and promote enhanced coverage in the state-action space.
- Our experiments on various challenging tasks demonstrate that SI2E significantly improves final performance and sample efficiency by up to 37.63% and 60.25%, respectively, compared to state-of-the-art baselines.

2 Preliminaries

In this section, we formalize the definitions of fundamental concepts. The descriptions of primary notations are summarized in Appendix A.1 for ease of reference.

2.1 Traditional Information Principles

Consider the random variable pair $Z = (X, Y)$ with a joint distribution probability denoted by $p(x, y) \in (0, 1)$. The marginal probabilities, $p(x)$ and $p(y)$, are defined as $p(x) = \sum_y p(x, y)$ and $p(y) = \sum_x p(x, y)$, respectively. The joint Shannon entropy [Shannon, 1953] of X and Y is $H(X, Y) = -\sum_{(x,y)} [p(x, y) \cdot \log p(x, y)]$, which quantifies the total uncertainty in Z . Conversely, the marginal entropies $H(X) = -\sum_x [p(x) \cdot \log p(x)]$ and $H(Y) = -\sum_y [p(y) \cdot \log p(y)]$ characterize the uncertainty in X and Y individually. The mutual information $I(X; Y) = \sum_{x,y} \left[p(x, y) \cdot \log \frac{p(x,y)}{p(x)p(y)} \right]$ quantifies the shared uncertainty between X and Y . It satisfies the following relationship: $I(X; Y) = H(X) + H(Y) - H(X, Y)$.

2.2 Reinforcement Learning

Within the context of RL, the sequential decision-making problem is formalized as a Markov Decision Process (MDP) [Bellman, 1957]. The MDP is characterized by a tuple $(\mathcal{O}, \mathcal{A}, \mathcal{P}, \mathcal{R}^e, \gamma)$, where \mathcal{O} denotes the observation space, \mathcal{A} the action space, \mathcal{P} the environmental transition function, \mathcal{R}^e the extrinsic reward function, and $\gamma \in [0, 1)$ the discount factor. At each discrete timestep t , the agent selects an action $a_t \in \mathcal{A}$ upon observing $o_t \in \mathcal{O}$. This leads to a transition to a new observation $o_{t+1} \sim \mathcal{P}(o_t, a_t)$ and a reward $r_t^e \in \mathbb{R}$. The policy network π is optimized to maximize the cumulative long-term expected discounted reward.

Maximum State Entropy Exploration. In environments with sparse rewards, agents are encouraged to explore the state space extensively, which can be incentivized by maximizing the Shannon entropy $H(S)$ of state variable S . When the prior distribution $p(s)$ is not available, the non-parametric k -nearest neighbors (k -NN) entropy estimator [Singh et al., 2003] is employed. For a given set of n independent and identically distributed samples from a d_x -dimensional space $\{x_i\}_{i=0}^{n-1}$, the entropy of variable X is estimated as follows:

$$\hat{H}_{KL}(X) = \frac{d_x}{n} \sum_{i=0}^{n-1} \log d(x_i) + C, \tag{1}$$

¹<https://github.com/SELGroup/SI2E>

where $d(x_i)$ is twice the distance from x_i to its k -th nearest neighbor, and C is a constant term.

Information Bottleneck Principle. In the supervised learning paradigm, representation learning aims to transform an input source X into a representation Z , targeted towards an output source Y . The Information Bottleneck (IB) principle [Tishby et al., 2000] refines this process by maximizing the mutual information $I(Z; Y)$ between Z and Y , capturing the relevant features of Y within Z . Concurrently, the IB principle imposes a complexity constraint by minimizing the mutual information $I(Z; X)$ between Z and X , effectively discarding irrelevant features. To balance these objectives, the IB principle utilizes a Lagrangian multiplier, facilitating a balanced trade-off between the richness of the representation and its complexity.

2.3 Structural Information Principles

The encoding tree T of an undirected and weighted graph $G = (V, E)$ is characterized as a rooted tree with the following properties: 1) Each tree node α in T corresponds to a subset of graph vertices $V_\alpha \subseteq V$. 2) The subset V_λ of tree root λ encompasses all vertices in V . 3) Each subset V_ν of a leaf node ν in T only contains a single vertex v , thus $V_\nu = \{v\}$. 4) For each non-leaf node α , the number of its children is assumed as l_α , with the i -th child specified as α_i . The collection of subsets $V_{\alpha_1}, \dots, V_{\alpha_{l_\alpha}}$ constitutes a sub-partition of V_α .

Given an encoding tree T whose height is at most K , the K -dimensional structural entropy of graph G is defined as follows:

$$H^T(G) = - \sum_{\alpha \in T, \alpha \neq \lambda} \left[\frac{g_\alpha}{\text{vol}(G)} \cdot \log \frac{\text{vol}(\alpha)}{\text{vol}(\alpha^-)} \right], \quad H^K(G) = \min_T H^T(G), \quad (2)$$

where g_α is the weighted sum of all edges connecting vertices within the subset V_α to vertices outside the subset V_α .

3 Structural Mutual Information

In this section, we address the single-variable constraint prevalent in existing structural information principles and introduce the concept of structural mutual information for subsequent state-action representation learning within our SI2E framework.

Given the random variable pair (X, Y) with $|X| = |Y| = n$, we construct an undirected bipartite graph G_{xy} to represent the joint distribution of X and Y . In G_{xy} , each vertex $x \in X$ connects to each vertex $y \in Y$ via weighted edges, where the weight of each edge equals the joint probability $p(x, y)$. Notably, no edges connect vertices within the same set, X or Y , and the total sum of the edge weights is 1, $\sum_{x,y} p(x, y) = 1$. Each single-step random walk in G_{xy} accesses either a vertex from X or Y . The structural entropy of variable X in G_{xy} is defined as the number of bits required to encode all accessible vertices in the set X . It is calculated using the following formula:

$$H^{SI}(X) = - \sum_{x \in X} \left[\frac{p(x)}{\text{vol}(G_{xy})} \cdot \log \frac{p(x)}{\text{vol}(G_{xy})} \right] = - \sum_{x \in X} \left[\frac{p(x)}{2} \cdot \log \frac{p(x)}{2} \right], \quad (3)$$

where the sum of all vertex degrees is twice the total sum of edge weights, resulting in $\text{vol}(G_{xy}) = 2$.

The structural entropy $H^{SI}(Y)$ is defined similarly. We restrict the partitioning structure of G_{xy} to 2-layer approximate binary trees, denoted as \mathcal{T}^2 , to calculate the required bits to encode accessible vertices in X or Y , defined as the joint structural entropy. This tree structure mandates that each intermediate node (neither root nor leaf) has precisely two children. We begin by initializing a one-layer encoding tree, T_{xy}^0 , designating each non-root node α 's parent as the root λ , with $\alpha^- = \lambda$. By applying the stretch operator from the HCSE algorithm [Pan et al., 2021], we pursue an iterative and greedy optimization of T_{xy}^0 , further detailed in Appendix A.2. The optimal encoding tree, T_{xy}^* , for G_{xy} and the joint entropy under T_{xy}^* are achieved through:

$$T_{xy}^* = \arg \min_{T \in \mathcal{T}^2} H^T(G_{xy}), \quad H^{T^*}_{xy}(X, Y) = H^{T^*}_{xy}(G_{xy}). \quad (4)$$

Utilizing 2-layer approximate binary trees as the structural framework ensures computational tractability and more complex structures will increase the cost of increased computational complexity, which can be prohibitive for practical applications.

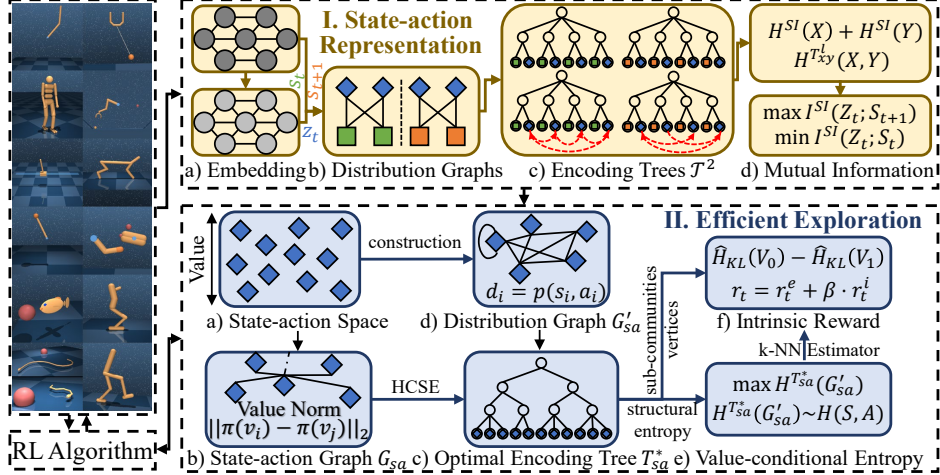


Figure 2: The SIZÉ’s overview architecture, including state-action representation learning and maximum structural entropy exploration.

We derive the following proposition regarding \mathcal{T}^2 , with the detailed proof provided in Appendix B.1.

Proposition 3.1. *Consider an undirected graph $G = (V, E)$ with vertices v_i and v_j in V . If the edge (v_i, v_j) is absent from E , then in the 2-layer approximate binary optimal encoding tree $T^* \in \mathcal{T}^2$, there does not exist any non-root node α such that both v_i and v_j are included in its subset V_α .*

Each intermediate node $\alpha \in T_{xy}^*$ corresponds to a subset T_α^* comprising exactly one x vertex and one y vertex, thus establishing a one-to-one matching structure between variables X and Y . The i -th intermediate node in T_{xy}^* , ordered from left to right, is denoted as α_i . Within this subset $T_{\alpha_i}^*$, the x and y vertices are labeled as x_i and y_i , respectively.

To define structural mutual information accurately, it is essential to consider the joint entropy of two variables under various partition structures. We introduce an l -transformation applied to T_{xy}^* to systematically traverse all potential one-to-one matching of these variables, providing a comprehensive measure of their structural similarity. Given an integer parameter $l > 0$, this transformation generates a new 2-layer approximate binary tree, T_{xy}^l , representing an alternative one-to-one matching structure.

Definition 3.2. For each intermediate node α_i in T_{xy}^l , the x and y vertices in $T_{\alpha_i}^l$ are specified as $T_{\alpha_i}^l = \{x_{i'}, y_{i'}\}$, where $i' = (i + l) \bmod n$.

The resulting tree T_{xy}^l is equivalent to the optimal tree T_{xy}^* when $l = 0$. We provide an example in Appendix A.3 with $n = 4$ for an intuitive understanding of the described process.

Definition 3.3. Leveraging the relationship $I(X; Y) = H(X) + H(Y) - H(X, Y)$ in traditional information theory, we formally define the structural mutual information, $I^{SI}(X; Y)$, as follows:

$$I^{SI}(X; Y) = \sum_{l=0}^{n-1} \left[H^{SI}(X) + H^{SI}(Y) - H^{T_{xy}^l}(X, Y) \right] = \sum_{i,j} \left[p(x_i, y_j) \cdot \log \frac{2}{p(x_i) + p(y_j)} \right]. \quad (5)$$

The detailed derivation is provided in Appendix C.1. Structural mutual information quantifies the average difference between the required encoding bits of accessible vertices of a single variable and the joint variable. The following theorem outlines the connection between $I^{SI}(X; Y)$ and $I(X; Y)$, with a detailed proof in Appendix B.2.

Theorem 3.4. *For a tuning parameter $0 \leq \epsilon \leq 1$, it holds for the structural mutual information $I^{SI}(X; Y)$, traditional mutual information $I(X; Y)$, and joint Shannon entropy $H(X, Y)$ that:*

$$I(X; Y) \leq I^{SI}(X; Y) \leq I(X; Y) + (1 - \epsilon) \cdot H(X, Y). \quad (6)$$

4 The Proposed SIZÉ Framework

In this section, we describe the detailed designs of the proposed SIZÉ framework, which captures dynamic-relevant state-action representations through structural mutual information (see Section

4.1) and enhances state-action coverage conditioned by the agent’s policy by maximizing structural entropy (see Section 4.2). The overall architecture of our framework is illustrated in Figure 2.

4.1 State-action Representation Learning

To effectively learn dynamics-relevant state-action representations, we present an innovative embedding principle that maximizes the structural mutual information with subsequent states and minimizes it with current states.

Structural Mutual Information Principle. In this phase, the input variables at timestep t encompass the current observation O_t and the action A_t , with the target being the subsequent observation O_{t+1} . We denote the encoding of observations O_t and O_{t+1} as states S_t and S_{t+1} , respectively. We aim to generate a latent representation Z_t for the tuple (S_t, A_t) , which preserves information relevant to S_{t+1} while compressing information pertinent to S_t . This embedding process mentioned above is detailed as follows:

$$S_t = f_s(O_t), \quad S_{t+1} = f_s(O_{t+1}), \quad Z_t = f_z(S_t, A_t), \quad (7)$$

where f_s and f_z are the respective encoders for states and state-action pairs (step I. a in Figure 2). For the state-action embeddings Z_t , we construct two undirected bipartite graphs, G_{zs} and $G_{zs'}$, as shown in step I. b of Figure 2. These graphs represent the joint distributions of Z_t with the current states S_t and subsequent states S_{t+1} . In step I. c of Figure 2, we generate 2-layer approximate binary trees for G_{zs} and $G_{zs'}$ and calculate the mutual information $I^{SI}(Z_t; S_t)$ and $I^{SI}(Z_t; S_{t+1})$ using Equation 5. Building upon the Information Bottleneck (IB) [Tishby et al., 2000], we present an embedding principle that aims to minimize $I^{SI}(Z_t; S_t)$ while maximizing $I^{SI}(Z_t; S_{t+1})$, as demonstrated in step I. d of Figure 2. When the joint distribution between variables Z_t and S_{t+1} shows a one-to-one correspondence-meaning for each $z_t \in Z_t$ value, there is a unique $s_{t+1} \in S_{t+1}$ corresponding to it, and vice versa-their mutual information takes its maximum value. We introduce a theorem to elucidate the equivalence between $I^{SI}(Z_t; S_{t+1})$ and $I(Z_t; S_{t+1})$ under this condition.

Theorem 4.1. *For a joint distribution of variables X and Y that shows a one-to-one correspondence, $I^{SI}(X; Y)$ equals $I(X; Y)$.*

A detailed proof is provided in Appendix B.3. When Z_t and S_t are mutually independent, the mutual information $I(Z_t; S_t)$ attains its minimum value. Our $I^{SI}(Z_t; S_t)$ goes beyond this, incorporating the joint entropy $H(Z_t, S_t)$ according to Theorem 3.4. This integration effectively eliminates the irrelevant information embedded in the representation variable Z_t , a significant step in our research. Consequently, structural mutual information can be considered a reasonable and desirable learning objective for acquiring dynamics-relevant state-action representations.

Representation Learning Objective. Due to the computational challenges of directly minimizing $I^{SI}(Z_t; S_t)$, we formulate a variational upper bound $I(Z_t; S_t) + H(Z_t|S_t) + H(S_t)$ (see Appendix C.2). Noting that the term $H(S_t)$ is extraneous to our model, we equate the minimization of $I^{SI}(Z_t; S_t)$ to the minimization of $I(Z_t; S_t)$ and $H(Z_t|S_t)$.

By employing a feasible decoder to approximate the marginal distribution of Z_t , we derive an upper bound of $I(Z_t; S_t)$ (See Appendix C.3) as follows:

$$I(Z_t; S_t) \leq \sum [p(z_t, s_t) \cdot D_{KL}(p(z_t|s_t)||q_m(z_t))] \triangleq L_{up}. \quad (8)$$

To concurrently decrease the conditional entropy $H(Z_t|S_t)$, we introduce a predictive objective (See Appendix C.4) through a tractable decoder $q_{z|s}$ for the conditional probability $p(z_t|s_t)$ as follows:

$$H(Z_t|S_t) \leq \sum \left[p(z_t, s_t) \cdot \log \frac{1}{q_{z|s}(z_t|s_t)} \right] \triangleq L_{z|s}, \quad (9)$$

where $L_{z|s}$ represents the log-likelihood of Z_t given S_t .

To efficiently optimize $I^{SI}(Z_t; S_{t+1})$, we maximize its lower bound, $I(Z_t; S_{t+1})$, as detailed in Theorem 3.4. By utilizing an alternative decoder $q_{s|z}$ for the conditional probability $p(s_{t+1}|z_t)$, we obtain a lower bound of $I(Z_t; S_{t+1})$ (See Appendix C.5) as follows:

$$I(Z_t; S_{t+1}) \geq \sum [p(z_t, s_{t+1}) \cdot \log q_{s|z}(s_{t+1}|z_t)] \triangleq L_{s|z}, \quad (10)$$

where $L_{s|z}$ denotes the log-likelihood of S_{t+1} conditioned on Z_t .

Within our SI2E framework, the definitive loss for representation learning is a combination of the above bounds, $L = L_{up} + L_{z|s} + \eta \cdot L_{s|z}$, where η is a Lagrange multiplier used to maintain equilibrium among the specified terms.

4.2 Maximum Structural Entropy Exploration

We have designed a unique intrinsic reward mechanism to address the challenge of imbalance exploration towards low-value states in traditional entropy strategies, as discussed by [Kim et al., 2023]. Specifically, we generate a hierarchical state-action structure based on the agent’s policy and define value-conditional structural entropy as an intrinsic reward for effective exploration.

Hierarchical State-action Structure. Derived from the history of agent-environment interactions, we extract state-action pairs (step II. a in Figure 2) to form a complete graph G_{sa} (step II. b in Figure 2) that encapsulates the value relationships caused by the agent’s policy. Within this graph, any two vertices v_i and v_j is connected by an undirected edge whose weight w_{ij} is determined as: $w_{ij} = \|\pi(s_t^i, a_t^i) - \pi(s_t^j, a_t^j)\|_2$. The state-action pairs (s_t^i, a_t^i) and (s_t^j, a_t^j) are associated with vertices v_i and v_j , respectively. We minimize the 2-dimensional structural entropy of this graph G_{sa} to generate its 2-layer optimal encoding tree, denoted as T_{sa}^* (step II. c in Figure 2). This tree T_{sa}^* delineates a hierarchical community structure among the state-action vertices, with the root node corresponding to a community encompassing all vertices. Each intermediate node in T_{sa}^* corresponds to a sub-community, including vertices that share similar π values.

Value-conditional Structural Entropy. To measure the extent of the policy’s coverage across the state-action space, we construct an additional distribution graph G'_{sa} (step II. d in Figure 2). The graph G'_{sa} shares the same vertex set as G_{sa} . The following proposition confirms the existence of such a graph, with a detailed proof provided in Appendix B.4.

Proposition 4.2. *Given positive visitation probabilities $p(s_t^0, a_t^0), \dots, p(s_t^{n-1}, a_t^{n-1})$ for all state-action pairs, there exists a weighted, undirected, and connected graph G'_{sa} , where each vertex’s degree d_i equals its visitation probability $p(s_t^i, a_t^i)$.*

In the graph G'_{sa} , the set of all state-action vertices is denoted as V_0 , and the set of all state-action sub-communities is denoted as V_1 . The Shannon entropies associated with the distribution of visitation probabilities for these sets are represented as $H(V_0)$ and $H(V_1)$, respectively, where $H(V_0) = H(S_t, A_t)$. Within the 2-layer state-action community represented by T_{sa}^* , we define the structural entropy of G'_{sa} using Equation 2, denoted as $H^{T_{sa}^*}(G'_{sa})$ (step II. e in Figure 2). The following theorem delineates the relationship between the value-conditional entropy $H^{T_{sa}^*}(G'_{sa})$ with the state-action Shannon entropy $H(S_t, A_t)$. A detailed proof is provided in Appendix B.5.

Theorem 4.3. *For a tuning parameter $0 \leq \zeta \leq 1$, it holds for the structural entropy $H^{T_{sa}^*}(G'_{sa})$ and the Shannon entropy $H(S_t, A_t)$ that:*

$$\zeta \cdot H(S_t, A_t) \leq H(V_0) - H(V_1) \leq H^{T_{sa}^*}(G'_{sa}) \leq H(S_t, A_t), \quad (11)$$

where $H(V_0) - H(V_1)$ is a variational lower bound of $H^{T_{sa}^*}(G'_{sa})$. On the one hand, the term $H(V_0)$ ensures maximal coverage of the entire state-action space, analogous to the traditional Shannon entropy. On the other hand, the term $H(V_1)$ mitigates uniform coverage among state-action sub-communities with diverse π values, thus addressing the challenge of imbalance exploration. By identifying the hierarchical state-action structure caused by the agent’s policy, the SI2E achieves enhanced maximum coverage exploration, thereby guaranteeing its exploration advantage.

Estimation and Intrinsic Reward. Considering the impracticality of directly acquiring visitation probabilities, we employ the k -NN entropy estimator in Equation 1 to estimate the lower bound:

$$H(V_0) - H(V_1) \approx \frac{d_z}{n_0} \cdot \sum_{i=0}^{n_0-1} \log d(v_i^0) - \frac{d_z}{n_1} \cdot \sum_{i=0}^{n_1-1} \log d(v_i^1) + C, \quad v_i^0 \in V_0, v_i^1 \in V_1, \quad (12)$$

where d_z is the dimension of state-action embedding, n_0 and n_1 are the vertex numbers in V_0 and V_1 , and $d(v)$ is twice the distance from vertex v to its k -th nearest neighbor. By ignoring the constant term in Equation 12, we define the intrinsic reward r_t^i and train RL agents to address the target task using a combined reward $r_t = r_t^e + \beta \cdot r_t^i$ (step II. f in Figure 2), where β is a positive hyperparameter that modulates the trade-off between exploration and exploitation. The pseudocode, complexity analysis, and limitations of our framework are provided in Appendix A.

Table 1: Summary of success rates and required steps to achieve target rewards in MiniGrid and MetaWorld tasks: “average value \pm standard deviation” and “average improvement”. **Bold**: the best performance, underline: the second performance.

MiniGrid Navigation	RedBlueDoors-6x6		SimpleCrossingS9N1		KeyCorridorS3R1	
	Success Rate (%)	Required Step (K)	Success Rate (%)	Required Step (K)	Success Rate (%)	Required Step (K)
A2C	-	-	88.18 \pm 3.46	570.08 \pm 15.87	86.57 \pm 2.26	658.74 \pm 21.03
A2C+SE	-	-	88.59 \pm 4.62	394.39 \pm 66.14	<u>87.20</u> \pm 4.94	463.86 \pm 38.27
A2C+VCSE	79.82 \pm 7.26	1161.90 \pm 241.59	91.30 \pm 1.92	204.02 \pm 25.60	86.01 \pm 0.91	190.20 \pm 6.11
A2C+SI2E	85.80 \pm 1.48	461.90 \pm 61.53	93.64 \pm 1.63	139.17 \pm 27.03	94.20 \pm 0.42	129.06 \pm 6.11
Abs.(%) Avg.	5.98(7.49) \uparrow	700.0(60.25) \downarrow	2.34(2.56) \uparrow	64.85(31.79) \downarrow	7.00(8.03) \uparrow	61.14(32.15) \downarrow
MiniGrid Navigation	DoorKey-6x6		DoorKey-8x8		Unlock	
	Success Rate (%)	Required Step (K)	Success Rate (%)	Required Step (K)	Success Rate (%)	Required Step (K)
A2C	92.67 \pm 8.47	567.20 \pm 96.57	-	-	92.48 \pm 11.96	669.78 \pm 154.74
A2C+SE	93.18 \pm 6.81	476.34 \pm 94.63	72.60 \pm 20.32	1515.81 \pm 324.28	91.34 \pm 18.37	634.37 \pm 240.51
A2C+VCSE	94.08 \pm 2.58	336.75 \pm 19.84	94.32 \pm 11.09	1900.96 \pm 398.65	93.12 \pm 3.43	405.22 \pm 52.22
A2C+SI2E	97.04 \pm 1.52	230.60 \pm 19.85	98.58 \pm 3.11	1090.96 \pm 125.77	97.13 \pm 3.35	309.14 \pm 53.71
Abs.(%) Avg.	2.96(3.15) \uparrow	106.15(31.52) \downarrow	4.26(4.52) \uparrow	424.85(28.03) \downarrow	4.01(4.31) \uparrow	96.08(23.71) \downarrow
MetaWorld Manipulation	Button Press		Door Open		Drawer Open	
	Success Rate (%)	Required Step (K)	Success Rate (%)	Required Step (K)	Success Rate (%)	Required Step (K)
DrQv2	94.55 \pm 4.64	105.0 \pm 5.0	-	-	-	-
DrQv2+SE	93.05 \pm 7.67	95.0 \pm 5.0	-	-	25.31 \pm 7.40	-
DrQv2+VCSE	89.80 \pm 3.29	77.5 \pm 2.5	80.90 \pm 10.19	-	82.74 \pm 7.46	175.0 \pm 5.0
DrQv2+SI2E	99.60 \pm 0.57	62.5 \pm 7.5	95.77 \pm 1.05	87.5 \pm 2.5	95.96 \pm 3.00	82.5 \pm 2.5
Abs.(%) Avg.	5.05(5.34) \uparrow	15.0(19.35) \downarrow	14.87(18.38) \uparrow	-	13.22(15.98) \uparrow	92.5(52.86) \downarrow
MetaWorld Manipulation	Faucet Close		Faucet Open		Window Open	
	Success Rate (%)	Required Step (K)	Success Rate (%)	Required Step (K)	Success Rate (%)	Required Step (K)
DrQv2	53.33 \pm 1.92	-	-	-	88.18 \pm 1.50	192.5 \pm 2.5
DrQv2+SE	92.36 \pm 3.66	71.25 \pm 6.25	-	-	93.14 \pm 2.03	172.5 \pm 2.5
DrQv2+VCSE	94.21 \pm 1.74	60.0 \pm 5.0	87.23 \pm 5.29	67.5 \pm 5.0	93.17 \pm 1.45	127.5 \pm 7.5
DrQv2+SI2E	99.37 \pm 1.18	27.5 \pm 2.5	97.06 \pm 1.39	51.25 \pm 3.75	99.46 \pm 0.35	77.5 \pm 2.5
Abs.(%) Avg.	5.16(5.48) \uparrow	32.5(54.17) \downarrow	9.83(11.27) \uparrow	16.25(24.07) \downarrow	6.29(6.75) \uparrow	50.0(39.22) \downarrow

5 Experiments

In this section, we present a comprehensive suite of comparative experiments on MiniGrid [Chevalier-Boisvert et al., 2018], MetaWorld [Yu et al., 2020], and the DeepMind Control Suite (DMControl) [Tunyasuvunakool et al., 2020] to evaluate the effectiveness of SI2E in terms of both final performance and sample efficiency. Consistent with previous work [Zeng et al., 2023c], we measure the required steps to attain specified rewards (0.9 times SI2E’s convergence reward) as a benchmark for assessing sample efficiency. For the SI2E implementation, we employ a randomly initialized encoder optimized to minimize the combined loss L . All experiments are conducted with 10 different random seeds, and the learning curves are delineated in Appendix E.

5.1 MiniGrid Evaluation

Initially, we assess our framework on navigation tasks using the MiniGrid benchmark, which includes goal-reaching tasks in sparse-reward environments. This setting is partially observable: the agent receives a $7 \times 7 \times 3$ embedding of the immediate surrounding grid rather than the entire grid. For comparative purposes, we employ the A2C agent [Mnih et al., 2016] with Shannon entropy (SE) [Seo et al., 2021] and value-based state entropy (VCSE) [Kim et al., 2023] as our baselines. Table 1 (upper) displays the average values and standard deviations of success rates and required steps for various navigation tasks. The tasks encompass navigation with obstacles (SimpleCrossingS9N1), long-horizon navigation (RedBlueDoors, DoorKey, and Unlock), and long-horizon navigation with obstacles (KeyCorridorS3R1). The SI2E consistently exhibits enhanced final performance and sample efficiency across tasks, with an average success rate increase of 4.92%, from 89.97% to 94.40%, and an average decrease in required steps of 38.10%, from 635.65K to 393.47K. In the RedBlueDoors task, where baseline performances are inadequate, our SI2E significantly improves the success rate from 79.82% to 85.80% and reduces the required steps from 1161.90K to 461.90K.

5.2 MetaWorld Evaluation

We further evaluate the SI2E framework on visual manipulation tasks from the MetaWorld benchmark, which presents exploration challenges due to its large state space. We select the model-free DrQv2 algorithm as the underlying RL methodology. Adhering to the setup of [Seo et al., 2023], we employ the same camera configuration and normalize the reward with a scale of 1. We summarize the success rates and required steps for all exploration methods across six MetaWorld tasks in Table 1 (lower).

Table 2: Summary of average episode rewards for control tasks in DMControl, encompassing two cartpole tasks characterized by sparse rewards: “average value \pm standard deviation” and “average improvement” (absolute value(%)). **Bold**: the best performance, underline: the second performance.

Domain, Task	Hopper Stand	Cheetah Run	Quadruped Walk	Pendulum Swingup	Cartpole Balance	Cartpole Swingup
DrQv2	87.59 \pm 11.70	229.28 \pm 123.93	289.79 \pm 24.17	424.21 \pm 246.96	998.97 \pm 22.95	–
DrQv2+SE	313.39 \pm 94.15	228.82 \pm 126.21	<u>290.27</u> \pm 24.20	10.80 \pm 2.92	993.80 \pm 75.24	219.69 \pm 62.21
DrQv2+VCSE	711.32 \pm 30.84	<u>456.26</u> \pm 22.20	243.74 \pm 29.91	<u>824.17</u> \pm 99.59	<u>998.65</u> \pm 9.58	<u>707.76</u> \pm 50.38
DrQv2+MADE	717.09 \pm 112.94	366.59 \pm 53.74	262.63 \pm 23.92	672.11 \pm 34.63	996.16 \pm 40.60	704.18 \pm 41.75
DrQv2+SI2E (Ours)	797.17 \pm 53.21	464.08 \pm 29.32	399.51 \pm 29.05	885.50 \pm 38.28	999.58 \pm 2.97	795.09 \pm 90.49
Abs.(%) Avg. \uparrow	80.08(11.17)	7.82(1.71)	109.24(37.63)	61.33(7.44)	0.93(0.09)	87.33(12.34)

Our SI2E framework enables the DrQv2 agent to solve all tasks with an average success rate of 97.87 after an average of 64.79K environmental steps, significantly outperforming other baselines. Specifically, in the Door Open task, all baselines struggle to achieve a meaningful success rate with a satisfactory number of environmental steps. This result demonstrates the SI2E’s effectiveness in improving and accelerating agent exploration in challenging tasks with expansive state-action spaces.

5.3 DMControl Evaluation

Subsequently, we evaluate our framework across various continuous control tasks within the DMControl suite. As the foundational agent, we choose the same DrQv2 algorithm, which operates on pixel-based observations. We incorporate a state-action exploration baseline, MADE [Zhang et al., 2021b], for a more comprehensive comparison. We evaluate all exploration methods across six continuous control tasks, documenting the episode rewards in Table 2. Observations reveal that SI2E remarkably increases the mean episode reward in each DMControl task. Specifically, in the Cartpole Swingup task characterized by sparse rewards, our framework boosts the average reward from 707.76 to 795.09, resulting in a 12.34% improvement in the final performance. Moreover, we compare the sample efficiency of SI2E and the best-performing baseline in Appendix E.3.

These results not only demonstrate the effectiveness of SI2E in acquiring dynamics-relevant representations for state-action pairs but also highlight its potential to motivate agents to explore the state-action space. To better understand the rationality and advantage of the SI2E framework, we provide visualization experiments in Appendix E.4.

5.4 Ablation Studies

To further investigate the impact of two critical components within the SI2E framework, embedding principle (Section 4.1) and intrinsic reward mechanism (4.2), we perform ablation studies on MetaWorld and DMControl tasks, focusing on two distinct variants: (i) SI2E-DB, which utilizes the DB bottleneck [Bai et al., 2021] for learning state-action representations, and (ii) SI2E-VCSE, employing the state-of-the-art VCSE approach [Kim et al., 2023] for calculating intrinsic rewards. As depicted in Figure 3, SI2E surpasses all variants regarding final performance and sample efficiency. This outcome underscores the essential role of these critical components in conferring SI2E’s superior capabilities. Additional ablation studies for the parameters β and n are available in Appendix E.5.

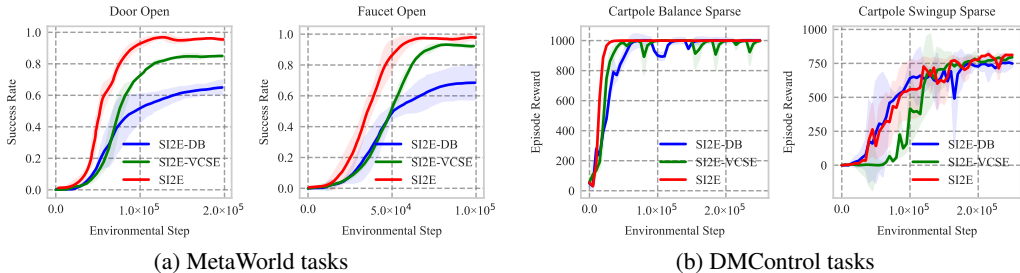


Figure 3: Learning curves across MetaWorld and DMControl tasks for ablation studies.

6 Related Work

6.1 Maximum Entropy Exploration

Maximum entropy exploration has evolved from focusing initially on unsupervised methods to incorporating task rewards in more advanced supervised models. In the unsupervised paradigm,

agents autonomously acquire behaviors by using state entropy as an intrinsic reward for exploration [Liu and Abbeel, 2021, Mutti et al., 2022, Yang and Spaan, 2023]. In contrast, in the supervised paradigm, agents aim to maximize state entropy in conjunction with task rewards [Seo et al., 2021, Yuan et al., 2022].

However, these methods face challenges due to imbalances in the distributions of states with differing policy values. To address this issue, a value-based approach [Kim et al., 2023] has been proposed, which integrates value estimates into the entropy calculation to ensure balanced exploration. Nevertheless, the effectiveness of this approach heavily depends on the partitioning structure of states according to policy values, requiring prior knowledge about downstream tasks.

In this work, we leverage structural information principles to derive the hierarchical state-action structure in an unsupervised manner. We further define the value-conditional structural entropy as an intrinsic reward to achieve more effective agent exploration. Compared to current maximum entropy explorations, SI2E introduces an additional sub-community entropy and minimizes this entropy to motivate the agent to explore specific sub-communities with high policy values. This approach helps avoid redundant explorations within low-value sub-communities and achieves enhanced maximum coverage exploration. Our method allows for balanced exploration without requiring prior knowledge of downstream tasks, effectively addressing the limitations of previous approaches.

6.2 Representation Learning

Novelty Search [Tao et al., 2020] and Curiosity Bottleneck [Kim et al., 2019b] leverage the Information Bottleneck principle for effective representation learning. Additionally, the EMI method [Kim et al., 2019a] maximizes mutual information in both forward and inverse dynamics to develop desirable representations. However, these methods are limited by the lack of an explicit mechanism to address the white noise issue in the state space. To overcome this challenge, the Dynamic Bottleneck model [Bai et al., 2021] is introduced for robust exploration in complex environments.

Our work defines structural mutual information to measure the structural similarity between two variables for the first time. Additionally, we present an innovative embedding principle that incorporates the entropy of the representation variable. This approach more effectively eliminates irrelevant information than the traditional information bottleneck principle.

6.3 Structural Information Principles

Since the introduction of structural information principles [Li and Pan, 2016], these principles have significantly transformed the analysis of network complexities, employing metrics such as structural entropy and partitioning trees. This innovative approach has not only deepened the understanding of network dynamics—even in the context of multi-relational graphs [Cao et al., 2024a]—but has also led to a wide array of applications across different domains. The application of structural information principles has extended to various fields, including graph learning [Wu et al., 2022], skin segmentation [Zeng et al., 2023a], and the analysis of social networks [Peng et al., Zeng et al., 2024, Cao et al., 2024b]. In the domain of reinforcement learning, these principles have been instrumental in defining hierarchical action and state abstractions through encoding trees [Zeng et al., 2023b,c], marking a significant advancement in robust decision-making frameworks.

7 Conclusion

We propose SI2E, a novel exploration framework based on structural information principles. This framework defines structural mutual information to effectively capture state-action representations relevant to environmental dynamics. It maximizes the value-conditional structural entropy to enhance coverage across the state-action space. We have established theoretical connections between SI2E and traditional information-theoretic methodologies, underscoring the framework’s rationality and advantages. Through extensive and comparative evaluations, SI2E significantly improves final performance and sample efficiency over state-of-the-art exploration methods. Our future work includes expanding the height of encoding trees and the range of experimental environments. Our goal is for SI2E to remain a robust and adaptable tool in reinforcement learning, particularly suited to high-dimensional and sparse-reward contexts.

Acknowledgments

The corresponding authors are Hao Peng and Angsheng Li. This work is supported by the National Key R&D Program of China through grant 2021YFB1714800, NSFC through grants 61932002, 62322202, and 62432006, Beijing Natural Science Foundation through grant 4222030, Local Science and Technology Development Fund of Hebei Province Guided by the Central Government of China through grant 246Z0102G, Hebei Natural Science Foundation through grant F2024210008, and Guangdong Basic and Applied Basic Research Foundation through grant 2023B1515120020.

References

- Abbas Abdolmaleki, Jost Tobias Springenberg, Yuval Tassa, Remi Munos, Nicolas Heess, and Martin Riedmiller. Maximum a posteriori policy optimisation. In *International Conference on Learning Representations*, 2018.
- Marcin Andrychowicz, Filip Wolski, Alex Ray, Jonas Schneider, Rachel Fong, Peter Welinder, Bob McGrew, Josh Tobin, OpenAI Pieter Abbeel, and Wojciech Zaremba. Hindsight experience replay. *Advances in neural information processing systems*, 30, 2017.
- Adrià Puigdomènech Badia, Bilal Piot, Steven Kapturowski, Pablo Sprechmann, Alex Vitvitskiy, Zhaohan Daniel Guo, and Charles Blundell. Agent57: Outperforming the atari human benchmark. In *International conference on machine learning*, pages 507–517. PMLR, 2020.
- Chenjia Bai, Lingxiao Wang, Lei Han, Animesh Garg, Jianye Hao, Peng Liu, and Zhaoran Wang. Dynamic bottleneck for robust self-supervised exploration. *Advances in Neural Information Processing Systems*, 34:17007–17020, 2021.
- Richard Bellman. A markovian decision process. *Journal of Mathematics and Mechanics*, pages 679–684, 1957.
- Yuwei Cao, Hao Peng, Angsheng Li, Chenyu You, Zhifeng Hao, and Philip S. Yu. Multi-relational structural entropy. In *The 40th Conference on Uncertainty in Artificial Intelligence*, pages 4289–4298, 2024a.
- Yuwei Cao, Hao Peng, Zhengtao Yu, and Philip S. Yu. Hierarchical and incremental structural entropy minimization for unsupervised social event detection. In *Proceedings of the AAAI Conference on Artificial Intelligence*, volume 38, pages 8255–8264, 2024b.
- Maxime Chevalier-Boisvert, Lucas Willems, and Suman Pal. Minimalistic gridworld environment for openai gym. 2018.
- Tuomas Haarnoja, Haoran Tang, Pieter Abbeel, and Sergey Levine. Reinforcement learning with deep energy-based policies. In *International conference on machine learning*, pages 1352–1361. PMLR, 2017.
- Tuomas Haarnoja, Aurick Zhou, Pieter Abbeel, and Sergey Levine. Soft actor-critic: Off-policy maximum entropy deep reinforcement learning with a stochastic actor. In *International conference on machine learning*, pages 1861–1870. PMLR, 2018.
- Elad Hazan, Sham Kakade, Karan Singh, and Abby Van Soest. Provably efficient maximum entropy exploration. In *International Conference on Machine Learning*, pages 2681–2691. PMLR, 2019.
- Riashat Islam, Raihan Seraj, Pierre-Luc Bacon, and Doina Precup. Entropy regularization with discounted future state distribution in policy gradient methods. *ArXiv*, 2019.
- Daejin Jo, Sungwoong Kim, Daniel Nam, Taehwan Kwon, Seungeun Rho, Jongmin Kim, and Donghoon Lee. Leco: Learnable episodic count for task-specific intrinsic reward. *Advances in Neural Information Processing Systems*, 35:30432–30445, 2022.
- Dongyoung Kim, Jinwoo Shin, Pieter Abbeel, and Younggyo Seo. Accelerating reinforcement learning with value-conditional state entropy exploration. *arXiv preprint arXiv:2305.19476*, 2023.

- Hyoungeok Kim, Jaekyeom Kim, Yeonwoo Jeong, Sergey Levine, and Hyun Oh Song. Emi: Exploration with mutual information. In *International Conference on Machine Learning*, pages 3360–3369. PMLR, 2019a.
- Youngjin Kim, Wontae Nam, Hyunwoo Kim, Ji-Hoon Kim, and Gunhee Kim. Curiosity-bottleneck: Exploration by distilling task-specific novelty. In *International conference on machine learning*, pages 3379–3388. PMLR, 2019b.
- Michael Laskin, Denis Yarats, Hao Liu, Kimin Lee, Albert Zhan, Kevin Lu, Catherine Cang, Lerrel Pinto, and Pieter Abbeel. Urlb: Unsupervised reinforcement learning benchmark. In *Deep RL Workshop NeurIPS 2021*, 2021.
- Angsheng Li and Yicheng Pan. Structural information and dynamical complexity of networks. *IEEE Transactions on Information Theory*, 62:3290–3339, 2016.
- Angsheng Li, Xianchen Yin, and Yicheng Pan. Three-dimensional gene map of cancer cell types: Structural entropy minimisation principle for defining tumour subtypes. *Scientific Reports*, 6:1–26, 2016.
- Hao Liu and Pieter Abbeel. Behavior from the void: Unsupervised active pre-training. *Advances in Neural Information Processing Systems*, 34:18459–18473, 2021.
- Yiwei Liu, Jiamou Liu, Zijian Zhang, Liehuang Zhu, and Angsheng Li. Rem: From structural entropy to community structure deception. *Advances in Neural Information Processing Systems*, 32:1–11, 2019.
- Volodymyr Mnih, Adria Puigdomenech Badia, Mehdi Mirza, Alex Graves, Timothy Lillicrap, Tim Harley, David Silver, and Koray Kavukcuoglu. Asynchronous methods for deep reinforcement learning. In *International conference on machine learning*, pages 1928–1937. PMLR, 2016.
- Mirco Mutti, Riccardo De Santi, and Marcello Restelli. The importance of non-markovianity in maximum state entropy exploration. In *International Conference on Machine Learning*, pages 16223–16239. PMLR, 2022.
- Ofir Nachum, Mohammad Norouzi, Kelvin Xu, and Dale Schuurmans. Bridging the gap between value and policy based reinforcement learning. *Advances in neural information processing systems*, 30, 2017.
- Aaron van den Oord, Yazhe Li, and Oriol Vinyals. Representation learning with contrastive predictive coding. *arXiv preprint arXiv:1807.03748*, 2018.
- Yicheng Pan, Feng Zheng, and Bingchen Fan. An information-theoretic perspective of hierarchical clustering. *arXiv preprint arXiv:2108.06036*, 2021.
- Deepak Pathak, Pulkit Agrawal, Alexei A Efros, and Trevor Darrell. Curiosity-driven exploration by self-supervised prediction. In *International conference on machine learning*, pages 2778–2787. PMLR, 2017.
- Hao Peng, Jingyun Zhang, Xiang Huang, Zhifeng Hao, Angsheng Li, Zhengtao Yu, and Philip S Yu. Unsupervised social bot detection via structural information theory. *ACM Transactions on Information Systems*, pages 1–42.
- Óscar Pérez-Gil, Rafael Barea, Elena López-Guillén, Luis M Bergasa, Carlos Gomez-Huelamo, Rodrigo Gutiérrez, and Alejandro Diaz-Diaz. Deep reinforcement learning based control for autonomous vehicles in carla. *Multimedia Tools and Applications*, 81(3):3553–3576, 2022.
- Sahaya Beni Prathiba, Gunasekaran Raja, Kapal Dev, Neeraj Kumar, and Mohsen Guizani. A hybrid deep reinforcement learning for autonomous vehicles smart-platooning. *IEEE Transactions on Vehicular Technology*, 70(12):13340–13350, 2021.
- Younggyo Seo, Lili Chen, Jinwoo Shin, Honglak Lee, Pieter Abbeel, and Kimin Lee. State entropy maximization with random encoders for efficient exploration. In *International Conference on Machine Learning*, pages 9443–9454. PMLR, 2021.

- Younggyo Seo, Danijar Hafner, Hao Liu, Fangchen Liu, Stephen James, Kimin Lee, and Pieter Abbeel. Masked world models for visual control. In *Conference on Robot Learning*, pages 1332–1344. PMLR, 2023.
- Claude Shannon. The lattice theory of information. *Transactions of the IRE professional Group on Information Theory*, 1(1):105–107, 1953.
- Harshinder Singh, Neeraj Misra, Vladimir Hnizdo, Adam Fedorowicz, and Eugene Demchuk. Nearest neighbor estimates of entropy. *American journal of mathematical and management sciences*, 23(3-4):301–321, 2003.
- Ruo Yu Tao, Vincent François-Lavet, and Joelle Pineau. Novelty search in representational space for sample efficient exploration. *Advances in Neural Information Processing Systems*, 33:8114–8126, 2020.
- Naftali Tishby, Fernando C Pereira, and William Bialek. The information bottleneck method. *arXiv preprint physics/0004057*, 2000.
- Saran Tunyasuvunakool, Alistair Muldal, Yotam Doron, Siqi Liu, Steven Bohez, Josh Merel, Tom Erez, Timothy Lillicrap, Nicolas Heess, and Yuval Tassa. dm_control: Software and tasks for continuous control. *Software Impacts*, 6:100022, 2020.
- Oriol Vinyals, Igor Babuschkin, Wojciech M. Czarnecki, and etc. Alphastar: Grandmaster level in starcraft ii using multi-agent reinforcement learning. *Nature*, 575(7782):350–354, 2019.
- Shanchuan Wan, Yujin Tang, Yingtao Tian, and Tomoyuki Kaneko. Deir: efficient and robust exploration through discriminative-model-based episodic intrinsic rewards. In *Proceedings of the Thirty-Second International Joint Conference on Artificial Intelligence*, pages 4289–4298, 2023.
- Junran Wu, Xueyuan Chen, Ke Xu, and Shangzhe Li. Structural entropy guided graph hierarchical pooling. In *ICML*, pages 24017–24030. PMLR, 2022.
- Qisong Yang and Matthijs TJ Spaan. Cem: Constrained entropy maximization for task-agnostic safe exploration. In *Proceedings of the AAAI Conference on Artificial Intelligence*, volume 37, pages 10798–10806, 2023.
- Zhenyu Yang, Ge Zhang, Jia Wu, Jian Yang, Quan Z Sheng, Hao Peng, Angsheng Li, Shan Xue, and Jianlin Su. Minimum entropy principle guided graph neural networks. In *Proceedings of the Sixteenth ACM International Conference on Web Search and Data Mining*, pages 114–122, 2023.
- Denis Yarats, Rob Fergus, Alessandro Lazaric, and Lerrel Pinto. Mastering visual continuous control: Improved data-augmented reinforcement learning. In *International Conference on Learning Representations*, 2021.
- Tianhe Yu, Deirdre Quillen, Zhanpeng He, Ryan Julian, Karol Hausman, Chelsea Finn, and Sergey Levine. Meta-world: A benchmark and evaluation for multi-task and meta reinforcement learning. In *Conference on robot learning*, pages 1094–1100. PMLR, 2020.
- Mingqi Yuan, Man-On Pun, and Dong Wang. Rényi state entropy maximization for exploration acceleration in reinforcement learning. *IEEE Transactions on Artificial Intelligence*, 2022.
- Guangjie Zeng, Hao Peng, Angsheng Li, Zhiwei Liu, Chunyang Liu, Philip S Yu, and Lifang He. Unsupervised skin lesion segmentation via structural entropy minimization on multi-scale superpixel graphs. In *IEEE ICDM*, pages 768–777, 2023a.
- Xianghua Zeng, Hao Peng, and Angsheng Li. Effective and stable role-based multi-agent collaboration by structural information principles. *Proceedings of the AAAI Conference on Artificial Intelligence*, (10):11772–11780, Jun. 2023b.
- Xianghua Zeng, Hao Peng, Angsheng Li, Chunyang Liu, Lifang He, and Philip S Yu. Hierarchical state abstraction based on structural information principles. In *IJCAI*, pages 4549–4557, 2023c.
- Xianghua Zeng, Hao Peng, and Angsheng Li. Adversarial socialbots modeling based on structural information principles. In *Proceedings of the AAAI Conference on Artificial Intelligence*, volume 38, pages 392–400, 2024.

- Chuheng Zhang, Yuanying Cai, Longbo Huang, and Jian Li. Exploration by maximizing rényi entropy for reward-free rl framework. In *Proceedings of the AAAI Conference on Artificial Intelligence*, volume 35, pages 10859–10867, 2021a.
- Tianjun Zhang, Paria Rashidinejad, Jiantao Jiao, Yuandong Tian, Joseph E Gonzalez, and Stuart Russell. Made: Exploration via maximizing deviation from explored regions. *Advances in Neural Information Processing Systems*, 34:9663–9680, 2021b.
- Ruijie Zheng, Xiyao Wang, Yanchao Sun, Shuang Ma, Jieyu Zhao, Huazhe Xu, Hal Daumé III, and Furong Huang. Taco: Temporal latent action-driven contrastive loss for visual reinforcement learning. *Advances in Neural Information Processing Systems*, 36, 2024.
- Dongcheng Zou, Hao Peng, Xiang Huang, Renyu Yang, Jianxin Li, Jia Wu, Chunyang Liu, and Philip S Yu. Se-gsl: A general and effective graph structure learning framework through structural entropy optimization. In *Proceedings of the ACM Web Conference 2023*, pages 499–510, 2023.

A Framework Details

A.1 Notations

Table 3: Glossary of Notations.

Notation	Description
$X; Y$	Random variables/Vertex Sets
$x; y$	Variable values/Vertices
p	Probability
$H; I$	Shannon entropy; Mutual information
$\mathcal{O}; \mathcal{A}$	Observation space; Action space
$O; S; A$	Observation, state, action variables/Vertex sets
$o; s; a$	Single observation, state, action/vertex
$z; Z$	Single embedding; Embedding variables
\mathcal{P}	Transition function
$r; \mathcal{R}$	Reward; Reward function
$\pi; \gamma; t$	Policy network; Discount factor; Timestep
$f; q$	Encoder; Decoder
G	Graph
$v; V$	Single vertex; Vertex set
$e; E; w$	Edge; Edge set; Edge weight
$\alpha; T$	Tree node; Encoding tree
$\lambda; \nu$	Root node; Leaf node
$H^T, H^K, H^{SI}; \Delta H$	Structural entropy; Entropy reduction
\mathcal{T}	Approximate binary trees
I^{SI}	Structural mutual information

A.2 Tree Optimization on \mathcal{T}^2

In this subsection, we have provided additional explanations and illustrative examples for the encoding tree optimization on \mathcal{T}^2 . As shown in Figure 4, the stretch operator is executed over sibling nodes α_i and α_j that share the same parent node, λ . The detailed steps of this operation are as follows:

$$\alpha_i^- = \lambda, \quad \alpha_i^- = \alpha', \quad \alpha_j^- = \alpha', \quad (13)$$

where α' is the added tree node via the stretch operation.

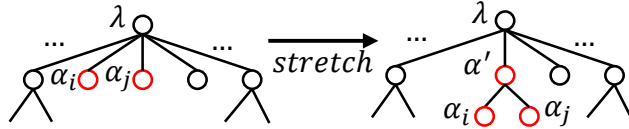


Figure 4: Stretch operation on sibling nodes within the encoding tree.

The corresponding variation in structural entropy, ΔH , due to the stretch operation is calculated as:

$$H^T(G; \alpha_i) = -\frac{g_{\alpha_i}}{\text{vol}(G)} \cdot \log \frac{\text{vol}(\alpha_i)}{\text{vol}(G)}, \quad H^T(G; \alpha_j) = -\frac{g_{\alpha_j}}{\text{vol}(G)} \cdot \log \frac{\text{vol}(\alpha_j)}{\text{vol}(G)}, \quad (14)$$

$$H^{T'}(G; \alpha_i) = -\frac{g_{\alpha_i}}{\text{vol}(G)} \cdot \log \frac{\text{vol}(\alpha_i)}{\text{vol}(\alpha')}, \quad H^{T'}(G; \alpha_j) = -\frac{g_{\alpha_j}}{\text{vol}(G)} \cdot \log \frac{\text{vol}(\alpha_j)}{\text{vol}(\alpha')}, \quad (15)$$

$$H^{T'}(G; \alpha') = -\frac{g_{\alpha'}}{\text{vol}(G)} \cdot \log \frac{\text{vol}(\alpha')}{\text{vol}(G)}, \quad (16)$$

$$\begin{aligned} \Delta H &= H^T(G; \alpha_i) + H^T(G; \alpha_j) - H^{T'}(G; \alpha_i) - H^{T'}(G; \alpha_j) - H^{T'}(G; \alpha') \\ &= (H^T(G; \alpha_i) - H^{T'}(G; \alpha_i)) + (H^T(G; \alpha_j) - H^{T'}(G; \alpha_j)) - H^{T'}(G; \alpha') \\ &= -\frac{g_{\alpha_i}}{\text{vol}(G)} \cdot \log \frac{\text{vol}(\alpha')}{\text{vol}(G)} - \frac{g_{\alpha_j}}{\text{vol}(G)} \cdot \log \frac{\text{vol}(\alpha')}{\text{vol}(G)} + \frac{g_{\alpha'}}{\text{vol}(G)} \cdot \log \frac{\text{vol}(\alpha')}{\text{vol}(G)} \\ &= -\frac{g_{\alpha_i} + g_{\alpha_j} - g_{\alpha'}}{\text{vol}(G)} \cdot \log \frac{\text{vol}(\alpha')}{\text{vol}(G)}. \end{aligned} \quad (17)$$

As shown in Algorithm 1, the HCSE algorithm iteratively and greedily selects the pair of sibling nodes that cause the maximum entropy variation, ΔH to execute one stretch optimization.

Algorithm 1 The Encoding Tree Optimization on \mathcal{T}^2

- 1: **Input:** one-layer initial encoding tree T
 - 2: **Output:** the optimal encoding tree $T^* \in \mathcal{T}^2$
 - 3: **while** True **do**
 - 4: $(\alpha_i, \alpha_j) \leftarrow$ maximize the entropy reduction ΔH caused by one stretch operation
 - 5: **if** $\Delta H = 0$ **then**
 - 6: Break
 - 7: **end if**
 - 8: Create a new tree node α'
 - 9: $(\alpha')^- \leftarrow \lambda, (\alpha_i)^- \leftarrow \alpha', (\alpha_j)^- \leftarrow \alpha'$
 - 10: **end while**
-

A.3 Intuitive Example of Optimal Encoding Tree

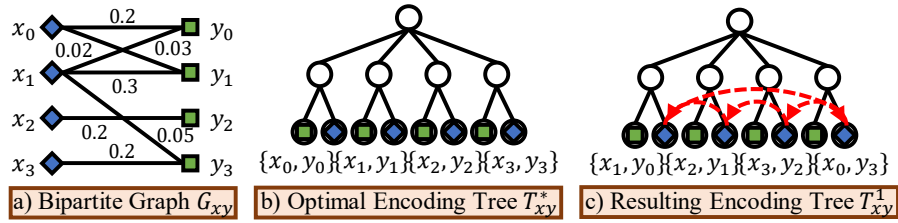


Figure 5: Illustration from a joint distribution to 2-layer approximate binary trees: a) Bipartite distribution graph, b) Optimal encoding tree, c) Resulting encoding tree via a 1-transformation.

A.4 The Pseudocode of SI2E

Algorithm 2 Effective Exploration based on Structural Information Principles

```

1: Input: batch size  $n$ , update interval  $t_{\text{up}}$ 
2: Initialize: agent's policy  $\pi$ , encoder functions  $f_s$  and  $f_z$ , decoder functions  $q_m, q_{z|s}, q_{s|z}$ , replay
   buffer  $\mathcal{B}$ 
3: for each episode do
4:   for each environmental step  $t$  do
5:     Collect transition  $\tau_t = (s_t, a_t, s_{t+1}, r_t^e)$  using the encoder  $f_s$  and policy  $\pi$ 
6:     Sample a batch  $\{\tau_{t_i}\}_{i=1}^n$  from  $\mathcal{B}$  including the variables  $S_t, A_t$ , and  $S_{t+1}$ 
7:     Adopt encoder functions  $f_z$  to obtain state-action embeddings  $Z_t$ 
8:     # Maximum Structural Entropy Exploration
9:     Construct the state-action graph  $G_{sa}$  according to the policy  $\pi$  and generate its hierarchical
   community structure  $T_{sa}^*$ 
10:    Employ the k-NN estimator to estimate the lower bound  $H(V_0) - H(V_1)$  and compute
   intrinsic reward  $r_t^i$ 
11:    Compute total reward  $r_t = r_t^e + \beta \cdot r_t^i$ 
12:    Update  $\tau_t' = (s_t, a_t, s_{t+1}, r_t)$  and augment  $\mathcal{B}$  with  $\tau_t'$ 
13:    if  $t \bmod t_{\text{up}} = 0$  then
14:      # Structural Mutual Information Principle
15:      Compute representation losses  $L_{\text{up}}, L_{z|s}$ , and  $L_{s|z}$ 
16:      Update encoder and decoder functions to minimize the combined loss  $L$ 
17:      Update agent policy  $\pi$  using  $\mathcal{B}$ 
18:    end if
19:  end for
20: end for

```

A.5 Complexity Analysis of SI2E

Within the SI2E framework, we analyze the time complexities of critical components independent of the underlying RL algorithm. During the state-action representation phase, the construction of bipartite graphs takes $O(n^2)$ time complexity, the generation of 2-layer approximate binary trees requires $O(n \cdot \log^2 n)$ time complexity, and the calculation of mutual information involves a time complexity of $O(n^2)$. During the effective exploration phase, the generation of hierarchical community structure incurs a $O(n \cdot \log^2 n)$ complexity, the construction of the distribution graph leads to a complexity of $O(n^2)$, and value-conditional structural entropy is calculated with $O(n)$ time complexity.

A.6 Limitations

Our work, which is a result of thorough research, aims to address the limitations of information theory methods and structural information theory research in reinforcement learning. Therefore, we have selected the state-of-the-art information theory exploration method as the baseline in our evaluation. Despite the current limitations in height due to complexity and cost issues, the encoding tree structure in the SI2E framework holds immense potential. In our future research, we are optimistic about expanding its height further and conducting more research on the advantages and restrictions brought by this expansion.

B Theorem Proofs

B.1 Proof of Proposition 3.1

Proof. For any two vertices $v_i \in V$ and $v_j \in V$ without any edge connecting them, their corresponding tree nodes are denoted as α_i and α_j . These nodes' parents are initially assigned as the root node λ . Before executing one stretch operation on vertices α_i and α_j , their structural entropies are calculated as follows:

$$H(G; \alpha_i) = -\frac{d_i}{\text{vol}(G)} \cdot \log \frac{d_i}{\text{vol}(G)}, \quad H(G; \alpha_j) = -\frac{d_j}{\text{vol}(G)} \cdot \log \frac{d_j}{\text{vol}(G)}, \quad (18)$$

where d_i and d_j are the degrees of vertices v_i and v_j . Post-stretch operation, their structural entropies are given by:

$$H(G; \alpha_i) = -\frac{d_i}{\text{vol}(G)} \cdot \log \frac{d_i}{\text{vol}(\alpha')}, \quad H(G; \alpha_j) = -\frac{d_j}{\text{vol}(G)} \cdot \log \frac{d_j}{\text{vol}(\alpha')}, \quad (19)$$

where α' are their new common parent node. The absence of an edge between v_i and v_j ensures that:

$$g_{\alpha'} = d_i + d_j, \quad \text{vol}(\alpha') = d_i + d_j. \quad (20)$$

The structural entropy of α' can be determined as:

$$H(G; \alpha') = -\frac{g_{\alpha'}}{\text{vol}(G)} \cdot \log \frac{\text{vol}(\alpha')}{\text{vol}(G)} = -\frac{d_i + d_j}{\text{vol}(G)} \cdot \log \frac{d_i + d_j}{\text{vol}(G)}. \quad (21)$$

The entropy reduction ΔH , consequent to the stretch operation on vertices v_i and v_j , is calculated as:

$$\begin{aligned} \Delta H &= \left[-\frac{d_i}{\text{vol}(G)} \cdot \log \frac{d_i}{\text{vol}(G)} - \frac{d_j}{\text{vol}(G)} \cdot \log \frac{d_j}{\text{vol}(G)} \right] \\ &\quad - \left[-\frac{d_i}{\text{vol}(G)} \cdot \log \frac{d_i}{d_i + d_j} - \frac{d_j}{\text{vol}(G)} \cdot \log \frac{d_j}{d_i + d_j} - \frac{d_i + d_j}{\text{vol}(G)} \cdot \log \frac{d_i + d_j}{\text{vol}(G)} \right] \\ &= \left[-\frac{d_i}{\text{vol}(G)} \cdot \log \frac{d_i}{\text{vol}(G)} - \frac{d_j}{\text{vol}(G)} \cdot \log \frac{d_j}{\text{vol}(G)} \right] - \left[-\frac{d_i}{\text{vol}(G)} \cdot \log \frac{d_i}{\text{vol}(G)} - \frac{d_j}{\text{vol}(G)} \cdot \log \frac{d_j}{\text{vol}(G)} \right] \\ &= 0. \end{aligned} \quad (22)$$

Given the zero reduction in entropy, as per lines 5 and 6 of the optimization algorithm for \mathcal{T}^2 (See Appendix A.2), the stretch operation involving v_i and v_j is omitted from the optimization process. \square

B.2 Proof of Theorem 3.4

Proof. The difference between the mutual information $I^{SI}(X; Y)$ and $I(X; Y)$ is expressed as:

$$\begin{aligned} I^{SI}(X; Y) - I(X; Y) &= \sum_{i,j} \left[p(x_i, y_j) \cdot \log \frac{2}{p(x_i) + p(y_j)} \right] - \sum_{i,j} \left[p(x_i, y_j) \cdot \log \frac{p(x_i, y_j)}{p(x_i) \cdot p(y_j)} \right] \\ &= \sum_{i,j} \left[p(x_i, y_j) \cdot \log \left[\frac{2}{p(x_i) + p(y_j)} \cdot \frac{p(x_i) \cdot p(y_j)}{p(x_i, y_j)} \right] \right] \\ &= \sum_{i,j} \left[p(x_i, y_j) \cdot \log \left[\frac{1}{p(x_i, y_j)} \cdot \frac{2 \cdot p(x_i) \cdot p(y_j)}{p(x_i) + p(y_j)} \right] \right] \\ &= \sum_{i,j} \left[p(x_i, y_j) \cdot \log \left[\frac{1}{p(x_i, y_j)} \cdot \frac{2}{\frac{1}{p(x_i)} + \frac{1}{p(y_j)}} \right] \right]. \end{aligned} \quad (23)$$

Given the conditions $p(x_i, y_j) \leq p(x_i) \leq 1$ and $p(x_i, y_j) \leq p(y_j) \leq 1$, the following inequalities are satisfied:

$$\frac{1}{p(x_i)} + \frac{1}{p(y_j)} \leq \frac{2}{p(x_i, y_j)}, \quad \frac{1}{p(x_i, y_j)} \cdot \frac{2}{\frac{1}{p(x_i)} + \frac{1}{p(y_j)}} \geq 1, \quad (24)$$

$$0 \leq \log_{p(x_i, y_j)} p(x_i) \leq 1, \quad 0 \leq \log_{p(x_i, y_j)} p(y_j) \leq 1. \quad (25)$$

By defining $\epsilon_i = \log_{p(x_i, y_j)} p(x_i)$ and $\epsilon_j = \log_{p(x_i, y_j)} p(y_j)$, we obtain the following results:

$$\begin{aligned} I^{SI}(X; Y) - I(X; Y) &= \sum_{i,j} \left[p(x_i, y_j) \cdot \log \left[\frac{1}{p(x_i, y_j)} \cdot \frac{2}{\left[\frac{1}{p(x_i, y_j)} \right]^{\epsilon_i} + \left[\frac{1}{p(x_i, y_j)} \right]^{\epsilon_j}} \right] \right] \\ &\leq (1 - \min(\epsilon_i, \epsilon_j)) \cdot \sum_{i,j} \left[p(x_i, y_j) \cdot \log \frac{1}{p(x_i, y_j)} \right] \\ &= (1 - \min(\epsilon_i, \epsilon_j)) \cdot H(X, Y). \end{aligned} \quad (26)$$

Therefore,

$$0 \leq I^{SI}(X; Y) - I(X; Y) \leq (1 - \min(\epsilon_i, \epsilon_j)) \cdot H(X, Y), \quad (27)$$

$$I(X; Y) \leq I^{SI}(X; Y) \leq I(X; Y) + (1 - \min(\epsilon_i, \epsilon_j)) \cdot H(X, Y). \quad (28)$$

□

B.3 Proof of Theorem 4.1

Proof. For a one-to-one correspondence of variables X and Y , the joint probability of a tuple (x_i, y_j) is as follows:

$$p(x_i, y_j) = \begin{cases} p(x_i) = p(y_j) & \text{if } i = j, \\ 0 & \text{otherwise.} \end{cases} \quad (29)$$

The calculation for $I^{SI}(X; Y)$ is carried out in the following manner:

$$\begin{aligned} I^{SI}(X; Y) &= \sum_{l=0}^n \left[H^{SI}(X) + H^{SI}(Y) - H^{T_{xy}^l}(X, Y) \right] \\ &= \sum_{i,j} \left[p(x_i, y_j) \cdot \log \frac{2}{p(x_i) + p(y_j)} \right] \\ &= \sum_i \left[p(x_i) \cdot \log \frac{1}{p(x_i)} \right] \\ &= H(X). \end{aligned} \quad (30)$$

Similarly, the calculation for $I(X; Y)$ proceeds as follows:

$$\begin{aligned} I(X; Y) &= \sum_{i,j} \left[p(x_i, y_j) \cdot \log \frac{p(x_i, y_j)}{p(x_i) \cdot p(y_j)} \right] \\ &= \sum_i \left[p(x_i) \cdot \log \frac{1}{p(x_i)} \right] \\ &= H(X). \end{aligned} \quad (31)$$

Hence, $I^{SI}(X; Y)$ equals $I(X; Y)$ when the joint distribution between X and Y shows a one-to-one correspondence. □

B.4 Proof of Proposition 4.2

Proof. Now, we employ mathematical induction to demonstrate the existence of the graph G'_{sa} .

Base Case ($n = 2$): Suppose the degree distribution of two vertices is given by (p_0, p_1) with $p_0 \leq p_1$.

We construct the graph G'_{sa} as follows:

- Create an edge with weight p_0 between v_0 and v_1 .
- Add a self-connected edge at vertex v_1 with weight $p_1 - p_0$.

Inductive Step ($n = k$): Assume that, the graph G'_{sa} with k vertices exists and satisfies Proposition 4.2.

Inductive Case ($n = k + 1$): Consider the addition of a new vertex v_k to construct G'_{sa} with $k + 1$

vertices using the following steps:

- Start with a subgraph that includes the first k vertices, yielding a distribution of (p'_0, \dots, p'_{k-1}) with $\sum_{i=0}^{k-1} p'_i = 1$.
- Modify the weight of all edges connected to each vertex v_i ($0 \leq i \leq k$) by a factor $\frac{(1-p_n)p_i}{p'_i}$.
- For each vertex v_i , create an edge with weight $p_i p_n$ connecting it to the new vertex v_k .
- Add a self-connected edge at vertex v_k with weight p_k^2 .

These modifications ensure that the degree distribution of the graph remains consistent with the addition of the new vertex, thus completing the inductive step and proving the existence of G'_{sa} for any n . \square

B.5 Proof of Theorem 4.3

In the tree T_{sa}^* , we denote the i -th intermediate node as α_i and its j -th child node as α_{ij} . The single state-action vertex in the corresponding subset of α_{ij} is assumed as (s_{ij}, a_{ij}) . In the graph G'_{sa} , the degree of any state-action vertex (s_{ij}, a_{ij}) is equated to its visitation probability, thereby:

$$\text{vol}(G'_{sa}) = \sum_{i,j} p(s_{ij}, a_{ij}) = 1, \quad \text{vol}(\alpha_{ij}) = g_{\alpha_{ij}} = p(s_{ij}, a_{ij}). \quad (32)$$

The 2-dimensional value-conditional structural entropy $H^{T_{sa}^*}(G'_{sa})$ is calculated through the following expressions:

$$\begin{aligned} H^{T_{sa}^*}(G'_{sa}) &= - \sum_i \left[g_{\alpha_i} \cdot \log \text{vol}(\alpha_i) + \sum_j \left[g_{\alpha_{ij}} \cdot \log \frac{\text{vol}(\alpha_{ij})}{\text{vol}(\alpha_i)} \right] \right] \\ &= - \sum_i \left[g_{\alpha_i} \cdot \log \text{vol}(\alpha_i) + \sum_j \left[p(s_{ij}, a_{ij}) \cdot \log \frac{p(s_{ij}, a_{ij})}{\text{vol}(\alpha_i)} \right] \right] \\ &= \sum_{i,j} \left[p(s_{ij}, a_{ij}) \cdot \log \frac{1}{p(s_{ij}, a_{ij})} \right] - \sum_i \left[\text{vol}(\alpha_i) \cdot \log \frac{1}{\text{vol}(\alpha_i)} \right] + \sum_i \left[g_{\alpha_i} \cdot \log \frac{1}{\text{vol}(\alpha_i)} \right] \\ &= H(V_0) - H(V_1) + \sum_i \left[g_{\alpha_i} \cdot \log \frac{1}{\text{vol}(\alpha_i)} \right] \\ &\geq H(V_0) - H(V_1). \end{aligned} \quad (33)$$

Given that $p(s_{ij}, a_{ij}) \cdot \text{vol}(\alpha_i) \leq p(s_{ij}, a_{ij}) \leq \text{vol}(\alpha_i)$, this inequalities hold that:

$$0 \leq \log_{p(s_{ij}, a_{ij})} \frac{p(s_{ij}, a_{ij})}{\text{vol}(\alpha_i)} \leq 1. \quad (34)$$

By defining $\zeta_{ij} = \log_{p(s_{ij}, a_{ij})} \frac{p(s_{ij}, a_{ij})}{\text{vol}(\alpha_i)}$, we obtain that:

$$\begin{aligned} \text{vol}(\alpha_i) \cdot \log \frac{1}{\text{vol}(\alpha_i)} &= \sum_j p(s_{ij}, a_{ij}) \cdot \frac{1}{\text{vol}(\alpha_i)} \\ &= \sum_j p(s_{ij}, a_{ij}) \cdot \log \frac{1}{[p(s_{ij}, a_{ij})]^{1-\zeta_{ij}}} \\ &= \sum_j \left[(1 - \zeta_{ij}) \cdot p(s_{ij}, a_{ij}) \cdot \log \frac{1}{p(s_{ij}, a_{ij})} \right]. \end{aligned} \quad (35)$$

Selecting the minimal ζ -value as ζ^* allow us to reformulate Equation 33 as follows:

$$H(V_1) = \sum_i \left[(\text{vol}(\alpha_i)) \cdot \log \frac{1}{\text{vol}(\alpha_i)} \right] \leq (1 - \zeta^*) \cdot H(S_t, A_t), \quad (36)$$

$$H(V_0) = H(S_t, A_t), \quad (37)$$

$$\zeta^* \cdot H(S_t, A_t) \leq H(V_0) - H(V_1) \leq H^{T_{sa}^*}(G'_{sa}) \leq H(S_t, A_t). \quad (38)$$

C Detailed Derivations

C.1 Derivation of $I^{SI}(X; Y)$

For each intermediate node $\alpha_i \in T_{xy}^*$ with vertex subset $\{x_i, y_i\}$, the entropy sum of this node and its children is calculated as follows:

$$\begin{aligned} & -\frac{g_{\alpha_i}}{\text{vol}(G_{xy})} \cdot \log \frac{\text{vol}(\alpha_i)}{\text{vol}(G_{xy})} - \frac{p(x_i)}{\text{vol}(G_{xy})} \cdot \log \frac{p(x_i)}{\text{vol}(\alpha_i)} - \frac{p(y_i)}{\text{vol}(G_{xy})} \cdot \log \frac{p(y_i)}{\text{vol}(\alpha_i)} \\ & = -\frac{g_{\alpha_i}}{2} \cdot \log \frac{\text{vol}(\alpha_i)}{2} - \frac{p(x_i)}{2} \cdot \log \frac{p(x_i)}{\text{vol}(\alpha_i)} - \frac{p(y_i)}{2} \cdot \log \frac{p(y_i)}{\text{vol}(\alpha_i)}. \end{aligned} \quad (39)$$

The $H^{SI}(X) + H^{SI}(Y) - H^{T_{xy}^*}(X, Y)$ term in Equation 5 is calculated as follows:

$$\sum_i \left[-\frac{p(x_i)}{2} \cdot \log \frac{p(x_i)}{2} - \frac{p(y_i)}{2} \cdot \log \frac{p(y_i)}{2} \right] - \sum_i \left[-\frac{g_{\alpha_i}}{2} \cdot \log \frac{\text{vol}(\alpha_i)}{2} - \frac{p(x_i)}{2} \cdot \log \frac{p(x_i)}{\text{vol}(\alpha_i)} - \frac{p(y_i)}{2} \cdot \log \frac{p(y_i)}{\text{vol}(\alpha_i)} \right]. \quad (40)$$

Proposition 3.1 ensures that:

$$\text{vol}(\alpha_i) = p(x_i) + p(y_i), \quad g_{\alpha_i} = p(x_i) + p(y_i) - 2p(x_i, y_i). \quad (41)$$

Consequently, we can reformulate Equation 40 as follows:

$$\begin{aligned} & \sum_i \left[\frac{p(x_i)}{2} \cdot \log \frac{2}{p(x_i) + p(y_i)} + \frac{p(y_i)}{2} \cdot \log \frac{2}{p(x_i) + p(y_i)} - \frac{p(x_i) + p(y_i) - 2 \cdot p(x_i, y_i)}{2} \cdot \log \frac{2}{p(x_i) + p(y_i)} \right] \\ & = \sum_i \left[p(x_i, y_i) \cdot \log \frac{2}{p(x_i) + p(y_i)} \right]. \end{aligned} \quad (42)$$

For any integer $l > 0$, the $H^{SI}(X) + H^{SI}(Y) - H^{T_{xy}^l}(X, Y)$ term in Equation 5 is given by:

$$\sum_i \left[p(x_{i'}, y_i) \cdot \log \frac{2}{p(x_{i'} + p(y_i))} \right], \quad i' = (i + l) \bmod n. \quad (43)$$

Consequently,

$$I^{SI}(X; Y) = \sum_{l=0}^n \left[H^{SI}(X) + H^{SI}(Y) - H^{T_{xy}^l}(X, Y) \right] = \sum_{i,j} \left[p(x_i, y_j) \cdot \log \frac{2}{p(x_i) + p(y_j)} \right]. \quad (44)$$

C.2 Upper Bound of $I^{SI}(Z_t; S_t)$

Theorem 3.4 assures the following inequality:

$$I^{SI}(X; Y) \leq I(X; Y) + (1 - \epsilon) \cdot H(X, Y), \quad 0 \leq \epsilon \leq 1. \quad (45)$$

Given the relationship between joint entropy and conditional entropy in traditional information theory, this inequality can be reformulated as follows:

$$\begin{aligned} I^{SI}(X; Y) & \leq I(X; Y) + (1 - \epsilon) \cdot H(X, Y) \\ & = I(X; Y) + (1 - \epsilon) \cdot H(X|Y) + (1 - \epsilon) \cdot H(Y) \\ & \leq I(X; Y) + H(X|Y) + H(Y). \end{aligned} \quad (46)$$

C.3 Upper Bound of $I(Z_t; S_t)$

Through the non-negativity of KL-divergence, the following upper bound of $I(Z_t; S_t)$ holds that:

$$\begin{aligned} I(Z_t; S_t) & = \sum \left[p(z_t, s_t) \cdot \log \frac{p(z_t|s_t)}{p(z_t)} \right] \\ & = \sum \left[p(z_t, s_t) \cdot \log \frac{p(z_t|s_t)}{q_m(z_t)} \right] - D_{KL}(p||q_m) \\ & \leq \sum [p(z_t, s_t) \cdot D_{KL}(p(z_t|s_t)||q_m(z_t))]. \end{aligned} \quad (47)$$

C.4 Upper Bound of $H(Z_t|S_t)$

Through the non-negativity of KL-divergence, the following upper bound of $H(Z_t|S_t)$ holds that:

$$\begin{aligned} H(Z_t|S_t) &= \sum \left[p(z_t, s_t) \cdot \log \frac{1}{p(z_t|s_t)} \right] \\ &= \sum \left[p(z_t, s_t) \cdot \log \frac{1}{q_{z|s}(z_t|s_t)} \right] - D_{KL}(p||q_{z|s}) \\ &\leq \sum \left[p(z_t, s_t) \cdot \log \frac{1}{q_{z|s}(z_t|s_t)} \right]. \end{aligned} \tag{48}$$

C.5 Lower Bound of $I(Z_t; S_{t+1})$

Leveraging the non-negative Shannon entropy and KL-divergence, we obtain the lower bound of $I(Z_t; S_{t+1})$:

$$\begin{aligned} I(Z_t; S_{t+1}) &= \sum \left[p(z_t, s_{t+1}) \cdot \log \frac{p(s_{t+1}|z_t)}{p(s_{t+1})} \right] \\ &= \sum [p(z_t, s_{t+1}) \cdot \log q_{s|z}(s_{t+1}|z_t)] + H(S_{t+1}) + D_{KL}(p||q_{s|z}) \\ &\geq \sum [p(z_t, s_{t+1}) \cdot \log q_{s|z}(s_{t+1}|z_t)]. \end{aligned} \tag{49}$$

D Experimental Details

In the experiments conducted for this work, we utilize a single NVIDIA RTX A1000 GPU and eight Intel Core i9 CPU cores clocked at 3.00GHz for each training run. The total number of environmental steps was set to 3000K/1000K for the MiniGrid benchmark, 200K/100K for the MetaWorld benchmark, and 250K for the DeepMind Control Suite (DMControl).

D.1 Implementation Details

A2C implementation details. In our implementation of the A2C algorithm, we utilize the official RE3 implementation², adhering to the pre-established hyperparameters set, except where explicitly noted. State representations in baselines are derived using a fixed encoder that is randomly initialized, and intrinsic rewards are normalized based on the standard deviation computed from sample data, consistent with the original methodology. However, this normalization process is omitted in the intrinsic reward calculations for VCSE and SI2E implementations. Across all exploration methods, we maintain fixed scale parameters $\beta = 0.005$ and $k = 5$, in line with the original framework. The comprehensive hyperparameters for the A2C algorithm are detailed in Table 4.

Table 4: Hyperparameters for the A2C algorithm on the MiniGrid benchmark.

Hyperparameter	Value
number of updates between two savings	100
number of processes	16
number of frames in training	3e6/1e6
scale parameter β	0.005
batch size	256
number of frames per process before update	5
discount factor	0.99
learning rate	0.001
GAE coefficient	0.95
maximum norm of gradient	0.5

DrQv2 implementation details. For the DrQv2 algorithm, we employ its official implementation³ [Yarats et al., 2021], maintaining the original hyperparameter settings unless specified otherwise. A fixed noise level of 0.2 and $k = 12$ are used for all exploration methods, including SE, VCSE, MADE, and SI2E. In the calculation of intrinsic rewards in baselines, we train the Intrinsic Curiosity Module [Pathak et al., 2017] using representations from the visual encoder to measure vertex distance in the estimation of value-conditional structural entropy. Specific hyperparameters in the DrQv2 are summarized in Table 5.

Table 5: Hyperparameters for the DrQv2 algorithm on the DeepMind Control Suite.

Hyperparameter	Value
number of frames stacked	3
number of times each action is repeated	2
number of frames for an evaluation	10000
number of episodes for each evaluation	10
number of worker threads for the replay buffer	4
replay buffer size	1e6
batch size	64
discount factor	0.99
learning rate	0.0001
feature dimensionality	50
hidden dimensionality	1024
scale parameter β	0.1

²<https://github.com/younggyoseo/RE3>

³<https://github.com/facebookresearch/drqv2>

D.2 Environment Details

MiniGrid Experiments. In our MiniGrid benchmark experiments, we encompass six navigation tasks, including RedBlueDoors, SimpleCorssingS9N1, KeyCorridor, DoorKey-6x6, DoorKey-8x8, and Unlock, with visual representations provided in Figure 6. Notably, all tasks are employed in their original forms without any modifications.

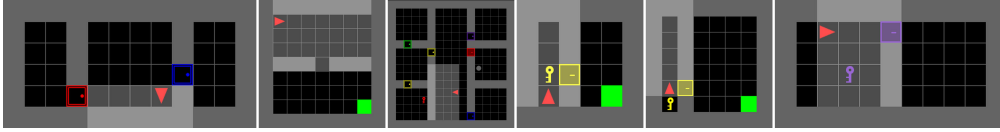


Figure 6: Examples of navigation tasks used in our MiniGrid experiments include: (a) RedBlueDoors, (b) SimpleCorssingS9N1, (c) KeyCorridor, (d) DoorKey-6x6, (e) DoorKey-8x8, (f) Unlock.

MetaWorld Experiments. In our evaluation using the MetaWorld benchmark, we conduct experiments on six manipulation tasks: Door Open, Drawer Open, Faucet Open, Window Open, Button Press, and Faucet Close. These tasks are visualized in Figure 7.

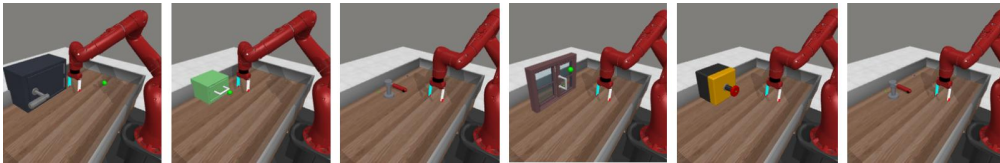


Figure 7: Examples of manipulation tasks used in our MetaWorld experiments include: (a) Door Open, (b) Drawer Open, (c) Faucet Open, (d) Window Open, (e) Button Press, (f) Faucet Close.

DMControl Experiments. Our research in DMControl suite focuses on six continuous control tasks, specifically Hopper Stand, Cheetah Run, Quadruped Walk, Pendulum Swingup, Cartpole Balance Sparse, and Cartpole Swingup Sparse. And visualizations of these tasks are provided in Figure 8.

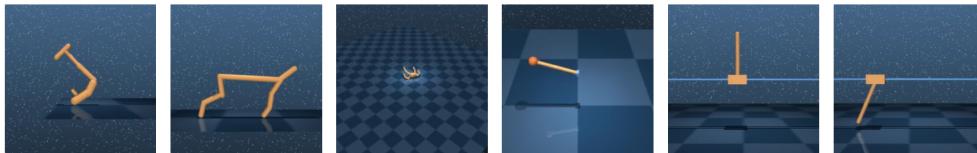


Figure 8: Examples of control tasks used in our DeepMind Control Suite experiments include: (a) Hopper Stand, (b) Cheetah Run, (c) Quadruped Walk, (d) Pendulum Swingup, (e) Cartpole Balance Sparse, (f) Cartpole Swingup Sparse.

E Additional Experiments

E.1 Experiments on MiniGrid Benchmark

Figure 9 illustrates the learning curves for the A2C algorithm integrated with our SI2E framework, as well as with other exploration baselines, SE and VCSE. The corresponding variants are labeled as A2C, A2C+SE, A2C+VCSE, and A2C+SI2E. These results demonstrate that SI2E consistently outperforms other baselines across various navigation tasks. In terms of final performance, A2C+SI2E achieves an average success rate of 94.40% across all navigation tasks, significantly outperforming the second-best A2C+VCSE, which has an average success rate of 89.78%. Regarding sample efficiency, SI2E converges in fewer than 50% of the total environmental steps in almost all tasks, except for DoorKey-8x8. This indicates SI2E’s effectiveness in enhancing the agent’s exploration of the state-action space, surpassing the baseline methods.

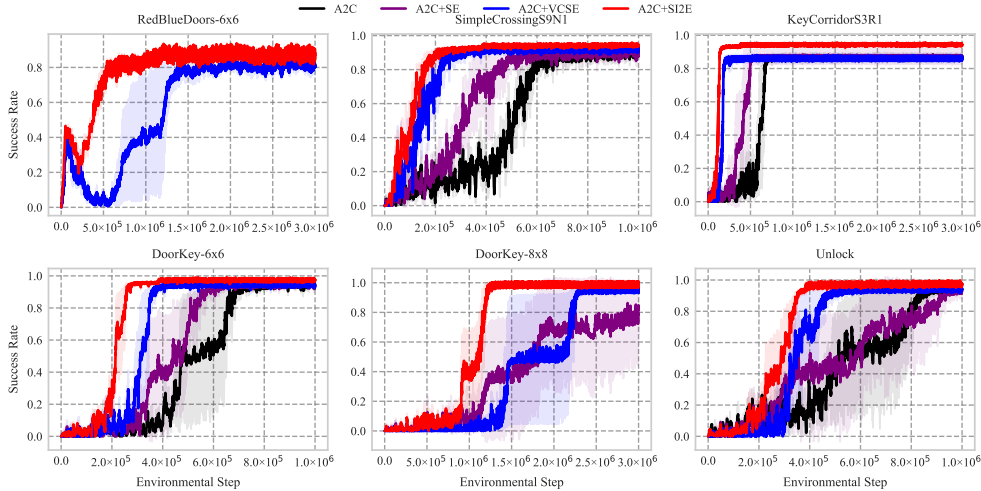


Figure 9: Learning curves for six navigation tasks in MiniGrid, measured in terms of success rate. The solid lines represent the interquartile mean, while the shaded regions indicate the standard deviation, both calculated across 10 runs.

To further substantiate our results on the Minigrd environment, we have introduced Leco[Jo et al., 2022] and DEIR[Wan et al., 2023], two additional state-of-the-art baselines representing advanced mechanisms for episodic intrinsic rewards. These results in Table 6 demonstrate that our method consistently maintains a performance advantage in terms of effectiveness and efficiency, even when compared to advanced episodic intrinsic reward mechanisms.

Table 6: Comparative results between SI2E and advanced episodic intrinsic reward mechanisms in MiniGrid benchmark: : “average value \pm standard deviation” and “average improvement”

MiniGrid Navigation	RedBlueDoors-6x6		SimpleCrossingS9N1		KeyCorridorS3R1	
	Success Rate (%)	Required Step (K)	Success Rate (%)	Required Step (K)	Success Rate (%)	Required Step (K)
Leco	81.97 \pm 10.81	817.47 \pm 137.21	90.02 \pm 4.13	417.59 \pm 17.63	90.36 \pm 0.57	520.43 \pm 10.31
DEIR	78.32 \pm 7.21	722.37 \pm 81.93	91.47 \pm 8.29	523.79 \pm 31.27	91.81 \pm 2.13	735.87 \pm 9.24
SI2E	85.80 \pm 1.48	461.90 \pm 61.53	93.64 \pm 1.63	139.17 \pm 27.03	94.20 \pm 0.42	129.06 \pm 6.11
MiniGrid Navigation	DoorKey-6x6		DoorKey-8x8		Unlock	
	Success Rate (%)	Required Step (K)	Success Rate (%)	Required Step (K)	Success Rate (%)	Required Step (K)
Leco	94.37 \pm 3.41	571.31 \pm 31.27	92.07 \pm 19.11	2168.35 \pm 293.52	94.48 \pm 6.39	791.40 \pm 82.39
DEIR	94.81 \pm 5.13	410.25 \pm 29.16	95.41 \pm 13.27	1247.58 \pm 231.42	95.13 \pm 12.74	531.06 \pm 131.84
SI2E	97.04 \pm 1.52	230.60 \pm 19.85	98.58 \pm 3.11	1090.96 \pm 125.77	97.13 \pm 3.35	309.14 \pm 53.71

E.2 Experiments on MetaWorld Benchmark

Figure 10 summarizes the learning curves for the DrQv2 algorithm with different exploration methods, including SI2E (ours), SE, and VCSE. These variants are denoted as DrQv2, DrQv2+SE, DrQv2+VCSE, and DrQv2+SI2E, respectively. As shown in Figure 10, SI2E consistently and significantly achieves higher success rates with fewer environmental steps across all manipulation tasks. On average, SI2E improves the final performance by 10.21% and sample efficiency by 45.06%.

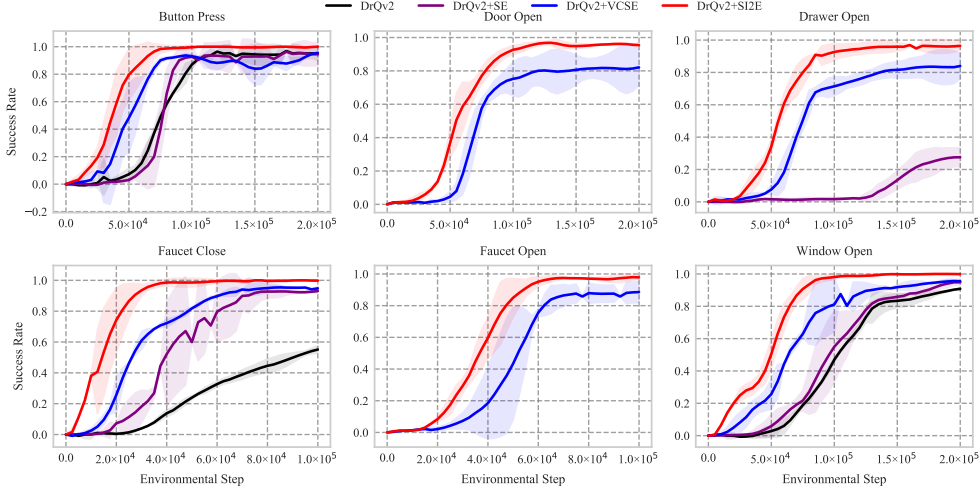


Figure 10: Learning curves for six manipulation tasks in MetaWorld, measured in terms of success rate. The solid lines represent the interquartile mean, while the shaded regions indicate the standard deviation, both calculated across 10 runs.

To provide additional validation, we conducted further experiments in the MetaWorld environment using the advanced TACO [Zheng et al., 2024] as the underlying agent. The new experimental results, as documented in Table 7, demonstrate the robustness and superior performance of our method with different underlying agents.

Table 7: Summary of success rates and required steps for the TACO agent in MetaWorld tasks: “average value \pm standard deviation” and “average improvement”. **Bold**: the best performance, underline: the second performance.

MetaWorld Manipulation	Button Press		Door Open		Drawer Open	
	Success Rate (%)	Required Step (K)	Success Rate (%)	Required Step (K)	Success Rate (%)	Required Step (K)
TACO	73.56 \pm 21.43	-	-	-	33.47 \pm 2.15	-
TACO+VCSE	91.43 \pm 5.51	95.0 \pm 5.0	78.59 \pm 4.22	-	70.93 \pm 6.65	-
TACO+SI2E	95.63 \pm 0.62	75.0 \pm 5.0	96.72 \pm 4.98	115.0 \pm 10.0	94.92 \pm 2.06	75.0 \pm 5.0
Abs.(%) Avg.	4.2(4.59) \uparrow	20.0(21.05) \downarrow	18.13(23.07) \uparrow	-	23.99(33.82) \uparrow	-
MetaWorld Manipulation	Faucet Close		Faucet Open		Window Open	
	Success Rate (%)	Required Step (K)	Success Rate (%)	Required Step (K)	Success Rate (%)	Required Step (K)
TACO	58.16 \pm 4.23	-	49.48 \pm 11.60	-	76.86 \pm 5.79	-
TACO+VCSE	76.00 \pm 0.75	-	80.40 \pm 3.65	-	92.31 \pm 3.17	120.0 \pm 5.0
TACO+SI2E	93.78 \pm 1.21	40.0 \pm 5.0	92.09 \pm 2.26	51.25 \pm 1.25	97.03 \pm 1.58	70.0 \pm 2.5
Abs.(%) Avg.	17.78(23.39) \uparrow	-	11.69(14.54) \uparrow	-	4.72(5.11) \uparrow	50.0(41.67) \downarrow

E.3 Experiments on DMControl Suite

For each task, we benchmark the convergence reward of the best-performing baseline as the target and track the environmental steps required by both SI2E and this baseline to reach the target. As illustrated in Figure 11, SISA demonstrates an average improvement of 35.60% in sample efficiency. This improvement is reflected in a reduction in the required environmental steps, decreasing from 31.83% to 20.5% of the total steps required to achieve the reward target.

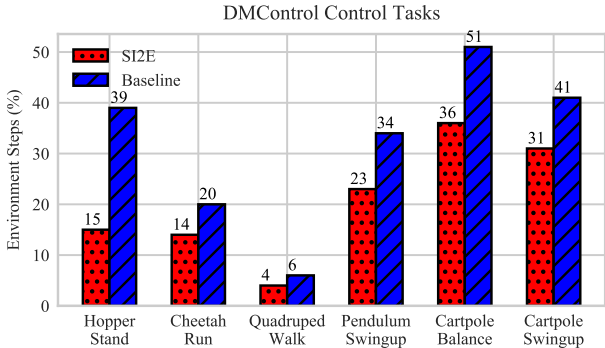


Figure 11: Comparison of sample efficiency between SI2E and the best-performing baseline in DMControl, focusing on the required environmental steps to reach the reward target, expressed as a proportion of the total 250K steps.

Figure 12 shows the learning curves for the DrQv2 algorithm when integrated with our SI2E framework and other exploration baselines, SE, VCSE, and MADE. The variants are identified as DrQv2, DrQv2+SE, DrQv2+VCSE, DrQv2+MADE, and DrQv2+SI2E. These results reveal that SI2E exploration significantly improves the sample efficiency of DrQv2 in both sparse reward and dense reward tasks, outperforming all other baselines. Particular in sparse reward tasks (Cartpole Balance and Cartpole Swingup), our framework successfully accelerates training and achieves higher episode rewards. This suggests that SI2E avoids exploring states that may not contribute to task resolution, thereby enhancing performance with a 5.17% improvement in final performance and a 15.28% increase in sample efficiency.

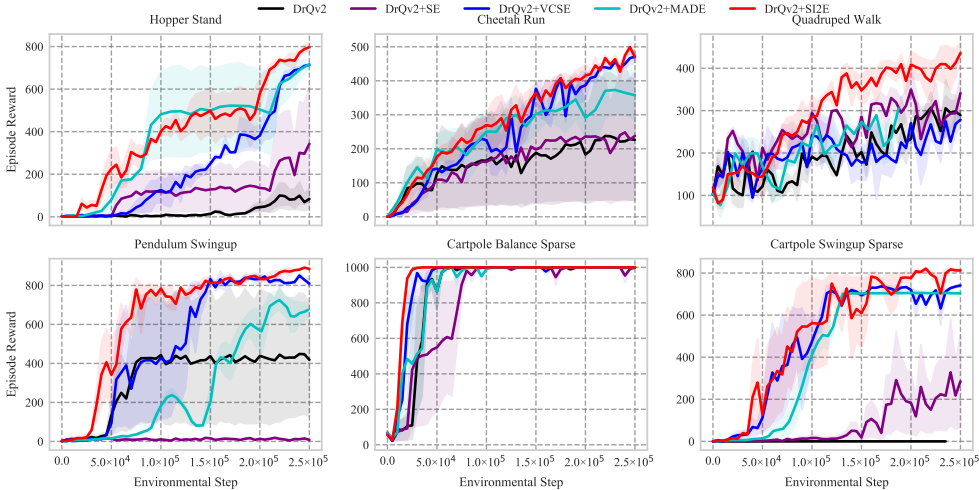


Figure 12: Learning curves for six continuous control tasks from DMControl Suite, measured in terms of episode reward. The solid lines represent the interquartile mean, while the shaded regions indicate the standard deviation, both calculated across 10 runs.

E.4 Visualization Experiment.

To understand the learned representation through our structural mutual information principle (Section 4.1), we use t-SNE to project the original observation O and state-action embedding Z into 2-dimensional vectors. Figure 13a visualizes these 2-dimensional vectors and measures the Euclidean distance between temporally consecutive vectors. Our presented principle aligns all movements on the same curve and reduces their distance by an average of 36.41, demonstrating its effectiveness for dynamics-relevant state-action embedding.

To analyze the benefits of our intrinsic reward mechanism (Section 4.2), we keep the map configuration constant in the SimpleCrossing task and display the exploration paths of various methods in Figure 13b. Our SI2E, in comparison to the SE and VCSE baselines, prevents biased exploration towards low-value areas and effectively explores high-value crucial areas, like the crossing point, with fewer environmental steps, ensuring its performance superiority.

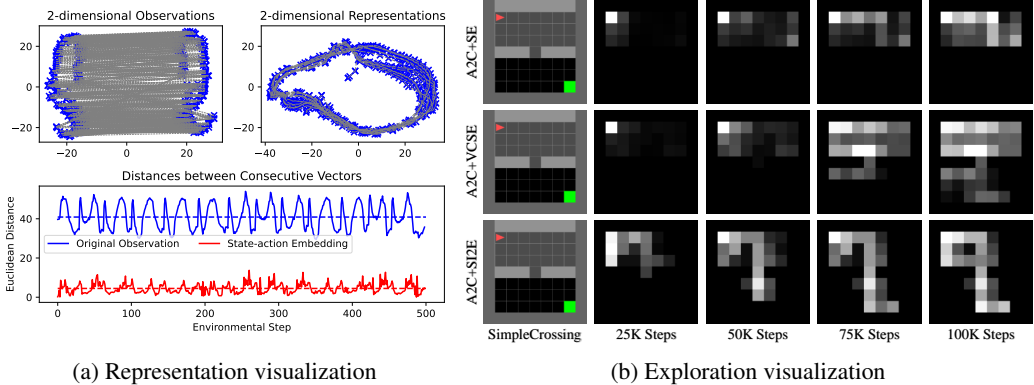


Figure 13: Visualization results of SI2E under DMControl and Minigrid tasks. (a) Visualization of representation learning based on structural mutual information principle. (b) Visualization of agent exploration through maximizing the value-conditional structural entropy.

Moreover, we have provided the visualizations of state coverage of our SI2E framework and other baselines (SE and VCSE) in the continuous Cartpole Balance task in Figure 14. Compared with the SE and VCSE baselines, our SI2E framework achieves a more efficient exploration strategy by minimizing occurrences in extreme positions and angles, resulting in a higher density in key areas.

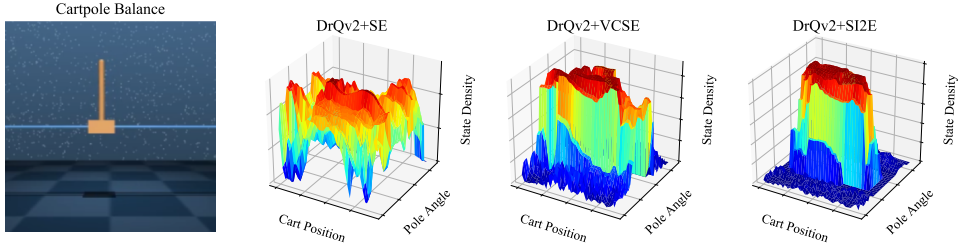


Figure 14: Visualization of agent exploration in the CartPole Balance task. Heat maps illustrate the final state densities for cart position and pole angle of the learned policies: (b)DrQv2+SE, (c) DrQv2+VCSE, and (d) DrQv2+SI2E.

E.5 Ablation Studies

To investigate the influence of parameters β and n on our framework’s performance, we incrementally adjust these parameters across two distinct tasks: DMControl tasks Hopper Stand and Pendulum Swingup. We meticulously document the resulting learning curves to assess the outcomes. Figure 15a illustrates that an increase in parameter β consistently enhances performance across both tasks, substantiating the effectiveness of our exploration method. Conversely, Figure 15b demonstrates that variations in batch size n yield comparable performance outcomes, particularly notable in Pendulum Swingup task, thereby confirming the SI2E’s stability amidst variations in batch size.

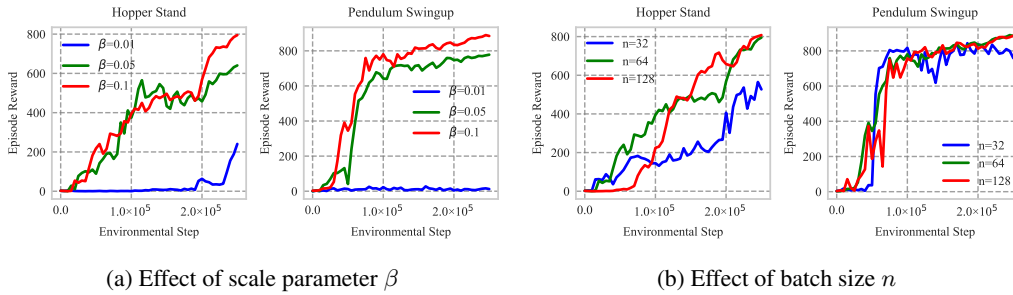


Figure 15: Learning curves of SI2E with varied β and n values on Hopper Stand and Pendulum Swingup tasks. (a) shows the effect of the scale parameter β on episode reward. (b) shows the effect of the batch size n on episode reward. The solid line represents the interquartile mean across 10 runs.